Non-linear effects in seismic waves in high-energy earthquakes: A two-dimensional analysis for non-homogeneous isotropic media with a view towards the study of the 2009 L'Aquila earthquake

Angelo Scrofani
Università degli studi di Sassari, Alghero, Italy

Giuliano Aretusi
Università degli Studi dell'Aquila, L'Aquila, Italy

Antonello Salvatori
Università degli Studi dell'Aquila, L'Aquila, Italy

Marco Tallini
Università degli Studi dell'Aquila, L'Aquila, Italy

Ivan Giorgio
Università degli Studi dell'Aquila, L'Aquila, Italy

Francesco D'Annibale
Università degli Studi dell'Aquila, L'Aquila, Italy

Francesco Fabbrocino
Pegaso-Università Telematica, Napoli, Italy

Luca Placidi
Università Telematica Internazionale UNINETTUNO, Roma, Italy

Abstract
It is usually accepted in geophysics (and in civil engineering) that linear models can be used for describing an earthquake and the consequent seismic waves' propagation. However, the large deformation experienced by the soil in these situations suggests that this paradigm requires more critical consideration. In fact, we claim that, in the vicinity of some discontinuities (that are common in all the geophysical applications of continuum models), the corresponding strain concentrations make the hypothesis of small deformation to be inadequate. In this paper, we verify the inappropriateness of the linear paradigm in a simple but reasonable case, with a view to a future application of this study to the effects of the 2009 L'Aquila earthquake. To this aim, we start with an analysis which is restricted to a two-dimensional body (i) with an inhomogeneity that resembles the Aterno River Valley, central Italy and (ii) with a non-linearity that is the most simple one, choosing the strain energy to be quadratic in the non-linear measures of deformation. More precisely, we consider a 2D piecewise homogeneous domain and a material that is viscoelastic isotropic and geometrically non-linear. We apply, to the bottom of such a domain, a seismic excitation and calculate the differences in the response between the linear and the geometrically non-linear cases. Using a suitably designed numerical model, we prove that, as conjectured, these differences not only originate near the pre-defined geometrical discontinuities but also propagate throughout the rest of the domain. Moreover, we find numerical predictions of the frequency ratios and ground acceleration time dependence and amplitude that produce, in the case of non-linear models, predictions which are closer to experimental evidence than those obtained using the corresponding linear model.

Keywords
Earthquake, waves, dynamics of soils, non-linear effects

1. Introduction

The current paradigm, usually accepted in geophysics, assumes that linear models can be used for describing the wave propagation consequent to tectonic or volcanics energy release, in what is called an earthquake. This paradigm is persistent, albeit more sophisticated non-linear studies in two- and three-dimensional domains, are widely present in the literature and deal with a wide class of mechan-ical phenomena [1–9] also related to the waves propagation [10–12]. For these types of applications of non-linear continuum mechanics , parameter identification represents a delicate point in the modelling process [13–17]. In the present paper, we will not try to get such an identification in the context of earthquakes modelling: instead we will explore the model's potentialities by means of a qualitative and semi-quantitative analysis, establishing the conceptual bases for further investigations.

While the linearised approach to earthquake dynamics and wave propagation, often linked to the forcing and free vibration of the structures [18–23], has produced very interesting and useful results, we claim that non-linear continuum mechanics gives a logical evidence that, in some specific instances, this approach cannot be accepted and must be modified. In particular, we state that when the medium in which the waves are propagating is strongly inhomogeneous, so that the fields of stiffnesses are suffering

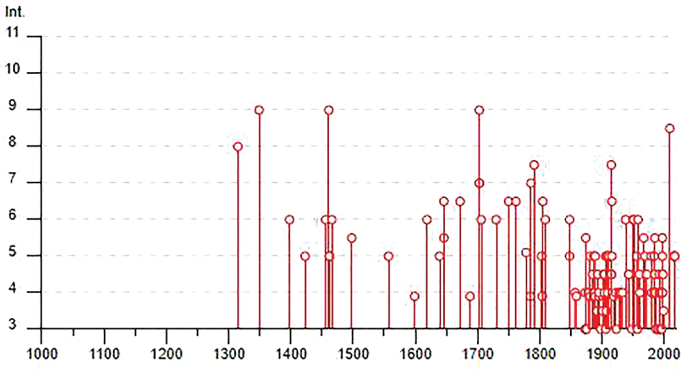

Figure 1. Macroseismic intensities relating to the city of L'Aquila plotted as time(years) vs intensity.

high gradients, and when the earthquake energy release is sufficiently high, then non-linear behaviour may become not negligible [24–27], also in the simplest case of purely geometrical non-linearities: to be more precise we remark here that, in the case examined in the numerical simulations of this paper, the released energy is estimated to be equivalent to the energy of an earthquake with a moment magnitude of 6, as described by Luca et al. [28]. As a consequence of our results, we urge for the introduction of more sophisticated non-linear models and numerical techniques, in order to get the required precise predictions of the earthquakes effects, especially when their energy is large. In this paper, the analysis is restricted to a two-dimensional case in order to get qualitative and preliminary quantitative information about the properties of considered mechanical systems and in order to prepare the more realistic three-dimensional analysis, which is needed to face the modelling problem arising when dealing with seismic propagation in the Aterno River Valley, where the city of L'Aquila is located. To make clearer the modelling challenges to be confronted we shortly recall, in what follow, the basic phenomenology whose modelling we intend to develop here and in our future planned investigations. The city of L'Aquila is located in the central part of the Apennine chain (central Italy), in a seismic area characterized by normal fault earthquakes [28,29]. This area (called "aquilano") has been struck in the past by numerous earthquakes such as those of 1315, 1349, 1461, 1703 and the recent one on 6 April 2009 (M_W6.3, [30] which macroseismic intensities up to XI on the Mercalli–Cancani–Sieberg scale (MCS), corresponding to an Ms close to 7 and causing deaths and damage; the Figure 1 shows the macroseismic intensities relating to the city of L'Aquila [31,32].

Before the 2009 event, the presence of seismic amplification in the city of L'Aquila was already known (within its historic walls) [33], and since then, numerous work were published on seismic microzonation [34–41], on strong motion data [42–47], on earthquake engineering [48–54], on damage distribution [53,55–57], on geological works [58–63], on geotechnical works ([43,64,65], and on numerical modeling ([46,66–72]. We remark that in Luca et al.'s study, [33] one can find a first attempt aimed to explain the observed seismic wave amplification effect (up to 10) in the 0.4–0.8 Hz frequency range. Of course, the 2009 L'Aquila earthquake has been largely discussed in the literature [30,33,44,69,71–73], and it is well-established that this geographic area shows different geological layers, as it was exposed already by Luca et al. [33], some years before of the seismic event that occurred in the city of L'Aquila in 2009. Always in Luca et al.'s study [33]: (1) some preliminary 1-D and 2-D linear continuum models for the superficial crust under the city of L'Aquila were introduced, and it was proven that, also by using such linear models, it can be forecast that the discontinuity of stiffnesses must greatly affect the ground accelerations, the frequency ratios and the seismic wave propagation velocities; (2)) some interesting experimental investigations in the urban area of the city were presented: in particular weak-motion data from earthquakes and ambient noise data were collected and analyzed. This experimental evidence given by weak-motion data share the same characteristics as the strong-motion records and shows clearly the presence of the amplification effect in the city. The geophysical model on which Luca et al. [33] is based proves that *the ground-motion amplification in the city of L'Aquila is related to the presence of a sedimentary basin, filled by lacustrine sediments, with a maximum depth of about* 250 *m*. Such area, situated in central Italy, is formed by NW-SE-dipping normal faults which produced rift valleys features typical to the intermontane basins

[74–77]. Several of these faults are still active and they may be responsible for further future earthquakes [78–81].

In this paper, we investigate the wave propagation in a two-dimensional continuous Cauchy medium caused by a forcing excitation, modelling the effects of high-energy earthquakes (moment magnitude higher than 6) originated at hypocenters far from the modelled region, where the seismic wave propagation is studied. In fact, the source of the seismic excitation in 2009 L'Aquila Earthquake was located 10km below the modelled region, whose thickness is about 1km: we explicitly remark that cannot use here the expression "deeper hypocenter", as the usual geological meaning of the term "deeper" in this context indicates that the hypocenter is located in the mantel under the crust. We consider, at first, linear models, that are models in which the deformation energy is assumed to be isotropic and quadratic in the linear deformation measure (i.e. the so-called infinitesimal strain tensor). Our aim, in this paper, is to prove that linear models are not fully capable to describe the phenomena occurring when it is necessary to consider continuous models featuring stiffness fields with high spatial gradients: this being the case when strongly non-homogeneous seismic wave propagation regions are to be considered [82–84]. In order to consider the simplest non-linear model, we introduce what is usually called a geometric non-linearity, by assuming that the isotropic deformation energy depends quadratically but on the finite strain tensor instead of depending on the linearised deformation measure [85]. We prove, with numerical simulations, that, the predictions of non-linear models dramatically differ from those obtained with linear models. These results seem to indicate, in particular in the case of the earthquakes propagating in the Aterno River Valley, that more sophisticated analyses are needed, if one wants to predict in a reliable way the effects of seismic waves on buildings and infrastructures. In fact, in the Aterno Valley, it is well-established that (see Luca et al. [33] and the references there cited) the ratio between the average stiffnesses observed in the soft alluvial sand or silt deposits layers and in the hard bedrock or calcareous breccia layer is, at least, one to four, so that high gradients of the stiffness fields are concentrated at the interface regions between these different layers or between the bedrock and the soft materials. It has to be remarked that in the literature also different modelling approaches have been attempted when considering linear or non-linear waves propagation. In fact, some discrete models based on lattice dynamics methods could be applied: see, for example Sharma and Eremeyev [86], Placidi et al. [87, 88] where transmission, refraction, and leakage of wave in the vicinity of surface defect were considered. Moreover, some surface-related phenomena in layered structures have been studied recently by Mikhasev et al. [89], where other references could be found. We believe, however, that the numerical implementation of continuum models, also in the presence of non-linearities, is so well-established and reliable that, at the moment, the approach which we used must be preferred. Because of the numerical simulations which we have performed, we have observed that the field of deformation (and kinetic) energy density difference between the linear and non-linear predictions, normalised with respect to the average deformation (and kinetic) energy in the non-linear case, starts being concentrated in the hard/soft interfaces at the beginning of the dynamic load (modelling the earthquake) and then propagates in both the soft and hard region: the amplitude of this propagating field may reach the values higher than 100% in a large region of the domain. Because of their applicative importance, the linear and non-linear acceleration field in several points close to the boundaries and their differences are calculated and discussed. The accelerations are normalised with respect to the gravity acceleration g and the difference between these two quantities can reach values around $0.77g$. We can conclude that the numerical evidence, which we have obtained, demands the development of more refined non-linear models for describing, in particular, the phenomenology observed in the city of L'Aquila during high-energy earthquakes. Albeit for the numerical simulations we have used the standard package included in COMSOL, some non-trivial encoding solutions have been used: (1)) the same finite-elements procedure has been used for solving simultaneously the linear and non-linear problem, (2)) a purely variational approach has been implemented, using suitable Hamilton conservative and Rayleigh dissipation functionals in the coding procedure, (3)) in order to avoid the reflection back inside the region of interest of the passing wave at its boundaries, we have chosen suitable optimal boundary conditions implementing viscoelastic displacement-force relationships at the lateral boundaries of the considered wave propagating region, while at its bottom a spherical displacement wave, originated in the hypocenter is imposed: the fact that the forcing action is originated by a far hypocenter is modelled by imposing at the basis of the bedrock a displacement calculated with a spherical wave transporting the required earthquake energy [90,91]. The very preliminary results, which we announce here, require the

development of a more sophisticated analysis in which: (1) isotropy hypothesis is relaxed; (2) the material elastic non-linearities are included in the modelling scheme; (3) the creep, damage, and plasticity effects are suitably accounted for; (4) the second-gradient deformation energy is postulated, for giving a better description of the boundary layers formed at the interfaces [92–100], also accounting for the change of the microstructure [101–104] and of the granular (and porous) nature of the soils [105–110] due to which strong local and macro-to-micro scale differences can be highlighted; (5)) the complete three-dimensional problem for the Aterno Valley is considered, in order to fully account for the peculiar behaviour experimentally observed by Luca et al. [33].

2. Geological setting of L'Aquila basin

In this section, we motivate our modeling assumptions based on the geological structure of the crust beneath the city of L'Aquila. It is located in a tectonic basin (Aterno river valley) bounded by a northwest-southeast-active normal fault ($https://diss.ingv.it/new-in-diss-3-3-0$), and it was founded in 1245, so that we have somehow detailed records about the seismic activity in its basic since then. The current tectonic setting of central Italy is due to the superposition of a previous a compressive phase (middle Oligocene - lower Pliocene, 28-3.6 Myr) during which the Apennine chain was created and the subsequent the post-orogenic extensional phase characterized by the origin of intermontane basins scattered in the central Apennine chain (such as L'Aquila basin - henceforth LAB in which is placed L'Aquila city) in the Messinian–Quaternary (7 Myr till now) [58,75–77]. LAB is placed in a NW-SE trending Plio-Quaternary intermontane tectonic basin bounded by SW dipping active normal fault accountable for the current and historical seismicity [31,81]. LAB is filled up by lacustrine, slope and alluvial deposits dated back from the upper Pliocene to the present (3.6 Myr till now) and laying via an unconformity surface onto the Messinian (7.2–5.3 Myr) terrigenous units and Meso-Cenozoic (100–70 and 20–12 Myr) carbonate units. LAB oldest post-orogenic deposits, made up by slope breccias and alluvial conglomerates, belong to the Colle Cantaro-Cave Formation (CCF) (upper Piacenzian-Gelasian 3.0–1.8 Myr) [61,77,111]. The Madonna della Strada Synthem (MDS), (in this study the soft layer) which is separated from the underlying CCF by an unconformity boundary, is made up by clayey–sandy silts and sands of Calabrian age (1.8–0.8 Myr) and referred to an alluvial meandering system within a wide and swampy flood plain [77]. Above MDS, separated by an unconformity boundary, the Middle Pleistocene (0.8–0.12 Myr) Fosso Genzano Synthem (FGS) is placed. It consists of gravels and sands referred to alluvial fans and plains [63]. The hill, where the L'Aquila historic downtown stands, is mainly made up by late Middle Pleistocene (0.3–0.12 Myr) calcareous breccias (in this study, the hard layer) which, via an erosive boundary, are superimposed on the underlying MDS and FGS deposits and the Meso-Cenozoic bedrock [112]. In fact, the historical part of the city (within the ancient walls) is placed on a fluvial terrace in the left bank of the Aterno River. The elevation of the terrace reaches 900 m a.s.l. (above mean sea level) in the NE part of the city and slopes down to 675 m in the SW direction. The terrace ends at the Aterno River which flows 50 m below yet. The terrace is made up of alluvial deposits created in the lower Quaternary age and is composed of breccias with limestone boulders and clasts in a marly matrix. The dimensions of these clasts can range from centimeters to some meters. This deposit is common in the Abruzzo region and may be related to catastrophic alluvial events associated with landslides [113]. These terrace were studied by Demageout [114], who named them "megabrecce". The "megabrecce" (called "mega breaches" in English) represents a well-defined geological unit with a thickness of some tens of meters. These deposits (megabrecce) are placed on the lacustrine sediments composed mainly of silty and sandy layers and minor gravel beds that can generate earthquakes with maximum expected magnitudes up to 6.5–7 [81]. The lacustrine sediments have their maximum thickness (around 300 m) in the center of the city of L'Aquila. In contrast, in the Aterno River valley, at north of L'Aquila, the thickness of the sediments is never greater than 100 m.

Further information about geological setting of L'Aquila basin will be exploited in future modelling efforts: in particular when 3D models will be used for getting the required predictions.

3. Modelling and coding assumption

In this section, we define univocally both the linear and non-linear models on the basis of which the analyses will be performed. The soil is modelled as a 2-dimensional domain and each of its material particles

will be characterised with the coordinate $\mathbf{X} = X_i\hat{\mathbf{e}}_i$ (where $\|\hat{\mathbf{e}}_i\| = 1$ and $i = 1, 2$) in a given reference configuration. The set of the kinematical descriptors, which depend upon the coordinates $\mathbf{X}$ and the time t, is composed of (1) the horizontal displacement $u_1\ (X_1, X_2, t)$ and (2) the vertical displacement $u_2\ (X_1, X_2, t)$. Let $\mathbf{u}(\mathbf{X}, t) = u_i\hat{\mathbf{e}}_i$ be the displacement vector of the generic point with X_i coordinates, $(\mathbf{X}, t)$ be the placement function, $\mathbb{F}$ be the deformation gradient tensor and $\mathbb{G}$ be the finite strain tensor. We will indicate with $\mathbf{x} = x_i\hat{\mathbf{e}}_i$ the coordinates in the current configuration, of the material point having coordinates $\mathbf{X}$ in the reference configuration. In formulae,

$$\mathbf{x} = \ (\mathbf{X}, t) = \mathbf{X} + \mathbf{u}, \qquad \mathbb{F} = \nabla\ , \qquad \mathbb{G} = \frac{1}{2}(\mathbb{F}^T\mathbb{F} - \mathbb{I}) \tag{1}$$

or, in index notation:

$$\Phi_i = X_i + u_i, \qquad F_{ij} = \frac{\partial \Phi_i}{\partial X_j} = u_{i,j} + \delta_{ij}, \qquad G_{ij} = \frac{1}{2}(F_{ki}F_{kj} - \delta_{ij}) \tag{2}$$

where

$$u_{i,j} = \frac{\partial u_i}{\partial X_j} \qquad \text{and} \qquad \delta_{ij} = \begin{cases} 1 & i = j \\ 0 & i \neq j \end{cases} \tag{3}$$

3.1. Deformation and kinetic energies and Rayleigh functional

Let $\mathcal{W}^{el}$ and $\mathcal{K}$ be the elastic internal deformation and the kinetic energies, respectively, and let $\partial_f\mathcal{B}$ be a subdomain of the boundary $\partial\mathcal{B}$ of the body $\mathcal{B}$ (see the Figure 2)

$$\mathcal{W}^{el} = \int_{\mathcal{B}} \left[\frac{1}{2}\lambda(tr\,\mathbb{G})^2 + \mu tr(\mathbb{G}^2)\right] dA + \int_{\partial_f\mathcal{B}} \frac{1}{2}K\mathbf{u}\cdot\mathbf{u}ds \tag{4}$$

$$\mathcal{K} = \int_{\mathcal{B}} \frac{1}{2}\rho\dot{\mathbf{u}}\cdot\dot{\mathbf{u}}dA \tag{5}$$

where λ and μ are the 2D Lamè coefficients and ρ is the mass density (per unit area) of the 2D domain, listed in Table 1, and K is the elastic stiffness per unit line of the bed of springs applied at the vertical boundaries $\partial_f B$, also listed in Table 1 (and shown in Figure 2). The dot between two vectors $\mathbf{a}$ and $\mathbf{b}$, denoted by $\mathbf{a}\cdot\mathbf{b}$, is their scalar product. Let the dissipation energy be:

$$\mathcal{W}^{dis} = \int_{\mathcal{B}} \mathcal{R}_{\mathcal{B}}dA + \int_{\partial_f\mathcal{B}} \mathcal{R}_f ds \tag{6}$$

and the two integrands have the following expression,

$$\mathcal{R}_{\mathcal{B}} = \frac{1}{2}\lambda_v(tr\,\dot{\mathbb{G}})^2 + \mu_v tr(\dot{\mathbb{G}}^2) \tag{7}$$

$$\mathcal{R}_f = \frac{1}{2}c\dot{\mathbf{u}}\cdot\dot{\mathbf{u}} \tag{8}$$

here, λ_v is a coefficient of viscosity and μ_v is the shear viscosity of the 2D domain, listed in Table 1 and c is the damping coefficient per unit line of the bed of dashpots applied at the vertical boundaries $\partial_f B$, also listed in Table 1. The Rayleigh dissipative term $\mathcal{R}_{\mathcal{B}}$, introduced in equation (7), acts within the domain, while the boundary dissipative term $\mathcal{R}_f$, defined in equation (8), mitigates non-physical wave reflections at the domain boundaries, as illustrated in Figure 2. Given that the domain represents a portion of soil, it

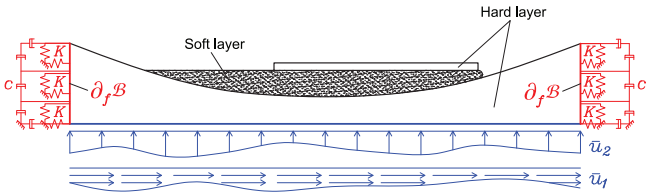

Figure 2. Boundary conditions: three boundary conditions were taken into account. On the two red lateral boundaries, indicating as $\partial_f\mathcal{B}$, are imposed a damping condition, derived from equation (19), and an elastic one, derived from equation (20). On the blue bottom boundary one has a boundary condition in terms of the displacements, see equations (32) and (33).

is reasonable to assume that seismic waves would naturally propagate beyond the model boundaries, dissipating into the surrounding soil mass. The linear approximation of the non-linear deformation defined at the third equation of (1) is given by

$$\mathbb{G} = \frac{1}{2}\left(\nabla\mathbf{u} + \nabla\mathbf{u}^T + \nabla\mathbf{u}^T\nabla\mathbf{u}\right) \quad \longrightarrow \quad \mathbb{E} = \frac{1}{2}\left(\nabla\mathbf{u} + \nabla\mathbf{u}^T\right). \tag{9}$$

So that in index notation we have

$$E_{ij} = \frac{1}{2}(u_{i,j} + u_{j,i}) \tag{10}$$

From the virtual work principle [115], indicating with t_1 and t_2 two different instants of time where the displacements $\mathbf{u}(\mathbf{X}, t_1)$ and $\mathbf{u}(\mathbf{X}, t_2)$ are known, the action is defined as a functional of the displacement function $\mathbf{u}(\mathbf{X}, t)$ as follows:

$$\mathcal{A}(u_1, u_2) = \int_{t_1}^{t_2} [\mathcal{W}^{el} - \mathcal{K}]dt \tag{11}$$

its first variation is:

$$\delta\mathcal{A} = \mathcal{A}(u_1 + \delta u_1, u_2 + \delta u_2) - \mathcal{A}(u_1, u_2) \tag{12}$$

By separately examining the two terms of equation (11), the variation (12) can be decomposed into the sum of the following quantities:

$$\int_{t_1}^{t_2} \delta\mathcal{W}^{el} = \int_{t_1}^{t_2} \frac{\partial\mathcal{W}^{el}}{\partial G_{ij}}\delta G_{ij}dt = \int_{t_1}^{t_2}\int_{\mathcal{B}} [\lambda G_{ii}\delta G_{jj} + 2\mu G_{ij}\delta G_{ij}]dAdt + \int_{t_1}^{t_2}\int_{\partial_f\mathcal{B}} Ku_i\delta u_i dsdt \tag{13}$$

and

$$\int_{t_1}^{t_2} \delta\mathcal{K}dt = \int_{t_1}^{t_2}\int_{\mathcal{B}} \rho\dot{\mathbf{u}}\cdot\delta\dot{\mathbf{u}}dAdt \tag{14}$$

Upon integration of equation (13) by parts, certain spatial boundary terms arise naturally. It is important to note that, following integration by parts, only on the boundary denoted by $\partial_f\mathcal{B}$ (see Figure 2) natural boundary conditions need to be added. This is because on the bottom blue boundary (see Figure 2), displacements (i.e. essential boundary conditions) are imposed, and therefore their variation is zero. Instead, integrating (14) by parts in time, we obtain

$$\begin{aligned}\int_{t_1}^{t_2} \delta\mathcal{K}dt &= \int_{t_1}^{t_2}\int_{\mathcal{B}} \frac{\partial}{\partial t}\left[\rho\dot{\mathbf{u}}\cdot\delta\mathbf{u}\right]dAdt - \int_{t_1}^{t_2}\int_{\mathcal{B}} \rho\ddot{\mathbf{u}}\cdot\delta\mathbf{u}dAdt \\ &= \int_{\mathcal{B}} \left[\rho\dot{\mathbf{u}}\cdot\delta\mathbf{u}\right]_{t_1}^{t_2} dA - \int_{t_1}^{t_2}\int_{\mathcal{B}} \rho\ddot{\mathbf{u}}\cdot\delta\mathbf{u}dAdt\end{aligned} \tag{15}$$

If the displacement at the times t_1 and t_2 are known and their variation $\delta\mathbf{u}$, for those instants of time, are equal to 0, then from equation (15) we have,

$$\int_{t_1}^{t_2} \delta\mathcal{K} dt = -\int_{t_1}^{t_2} \int_{\mathcal{B}} [\rho\ddot{\mathbf{u}} \cdot \delta\mathbf{u}]\, dA dt \tag{16}$$

The variation of the dissipative term $\mathcal{W}^{dis}$ in the equation (6) is defined as $\tilde{\delta}\mathcal{W}^{dis}$. The symbol of the variation operator we used for this quantity is different with respect total one present in equation (12) because such term is not a classic variation. The variation of the dissipative term is defined by the following expression:

$$\tilde{\delta}\mathcal{W}^{dis} = \int_{t_1}^{t_2} \left[\int_{\mathcal{B}} \frac{\partial \mathcal{R}_{\mathcal{B}}}{\partial \dot{G}_{ij}} \delta G_{ij} dA + \int_{\partial_f \mathcal{B}} \frac{\partial \mathcal{R}_f}{\partial \dot{u}_i} \delta u_i ds \right] dt \tag{17}$$

Also for equation (17) the integration by parts provides naturally the boundaries terms on $\partial_f\mathcal{B}$, where no kinematical restrictions are imposed. Finally, the variational principle is formulated as follows:

$$\delta\mathcal{A} + \tilde{\delta}\mathcal{W}^{dis} = 0 \tag{18}$$

for any admissible variation of the kinematic descriptors. On the red lateral boundaries (Figure 2) two different conditions are imposed: (1) a boundary damping constrain (as it is prescribed in the equation (8)) modeled as a bed of dashpots to avoid non-realistic reflections of the wave at the boundaries of the model. Some dissipation phenomena [116] may essentially change the wave propagation, see e.g. Eremeyev [117]. Insertion of equation (8) into equation (17) yields from equation (18) a standard dissipative force at the vertical boundary,

$$\int_{\partial\mathcal{B}} c\dot{\mathbf{u}} \cdot \delta\mathbf{u} ds. \tag{19}$$

and (2) a distributed force, modeled by means a bed of springs with stiffness equal to K and prescribed in the last boundary term of equation (4), to simulate the reaction of the lateral ground. Insertion of the last term of equation (4) into equation (11) yields from equation (18) a standard elastic force at the vertical boundary,

$$\int_{\partial\mathcal{B}} K\mathbf{u} \cdot \delta\mathbf{u} ds \tag{20}$$

3.2. The stiffness fields in the soft and hard region and kinematic boundary conditions

Based on the evidence made available, e.g., by Luca et al. [33], the region where seismic waves propagate is supposed to be constituted by two different materials, characterised by two different stiffnesses (the Young's moduli of the softest and the stiffest layers exhibit a 1/4 ratio as shown in the Table 1) and the 2D Lamè parameters were determined (the justification of the whole modelling procedure is similar to what done in Barchiesi et al. [118], to which we refer) using the following relationships for the plane stress case:

$$\lambda = \frac{Y\nu}{(1+\nu)(1-2\nu)},\ \mu = \frac{Y}{2(1+\nu)} \tag{21}$$

where Y represents the 2D Young's modulus and ν is the 2D Poisson coefficient. In the Table 1, we use the index s and h to denote that the parameter is linked either to the softer or to harder layers. The softer layer is located between the two harder layers as it is shown in Figure 2.

Clearly the distance $r(X_1, 0)$ of the generic point of the bottom boundary (blue part of the boundary in Figure 2), with coordinates $(X_1, 0)$ (with $X_1 \in [0, 7]$ km), from the hypocenter is:

$$r = \sqrt{(X_1 - X_{H1})^2 + (X_2 - X_{H2})^2} = \sqrt{(X_1 - X_{H1})^2 + X_{H2}^2} \tag{22}$$

Table 1. Material parameters that are used on the simulations. The indices *s* and *h* are linked with the layer in which the parameter is defined, respectively *softer* and *harder* one in Figure 2. Boundary parameters are also defined.

Soft domain	Hard domains	Boundary
$Y_s = 10\text{GPa}$	$Y_h = 40\text{GPa}$	$c = 10^8 \frac{\text{Ns}^2}{\text{m}^2}$
$\nu_s = 0.1$	$\nu_h = 0.25$	$K = 4.5 \frac{\text{N}}{\text{m}^2}$
$\lambda_{vs} = 5.2 \cdot 10^7 \text{Nms}^2$	$\lambda_{vh} = 2 \cdot 10^5 \text{Nms}^2$	
$\mu_{vs} = 1.44 \cdot 10^8 \text{Nms}^2$	$\mu_{vh} = 4 \cdot 10^5 \text{Nms}^2$	
$\rho_s = 1500 \frac{\text{kg}}{\text{m}^3}$	$\rho_h = 2700 \frac{\text{kg}}{\text{m}^3}$	

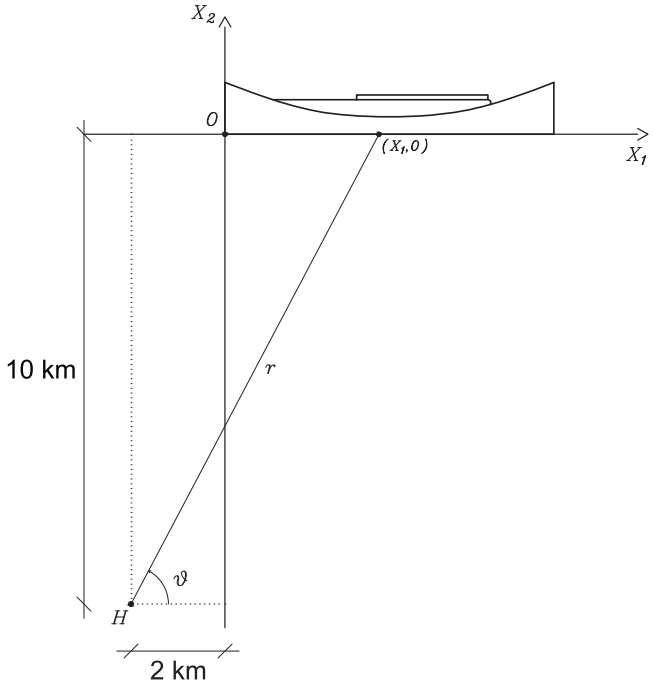

Figure 3. 2-D model: the body is modeled as a domain that consists of three main parts, in which two of these are harder then the other one. The seismic excitation starts at the hypocenter having coordinates $H \equiv (X_{H1}, X_{H2}) = (-2\text{km}, -10\text{km})$.

In the Figure 2, one can see how on the blu boundary at the bottom, the displacement $\bar{\mathbf{u}}$ is imposed for modelling the seismic action. The excitation originates from the hypocenter (point H in Figure 3), spreads into the ground until it reaches the "inhomogeneous superficial region" where wave propagation is analysed. The seismic excitation is assumed to last 3 seconds. Roughly speaking the imposed displacement is the result of the compositions of several waves (three longitudinal and three shear ones). To be more precise, the seismic excitation is modelled by means of the following simplifying assumptions: (1) it propagates as a spheric wave that diffuses, under the studied region of propagation, from an hypocenter H (see Figure 3), with coordinates $(X_{H1}, X_{H2}) = (-2\text{km}, -10\text{km})$, that resides beneath the domain of our investigation; (2)) it interacts with the inhomogeneous superficial region through the blu boundary by "imposing" its displacement; (3)) it does not affect the lateral boundary of the inhomogeneous superficial region, where only linear elastic conservative and dissipative interactions occur between the neighbouring parts of crust. This last modelling choice, of course, limits the quantitative predictability of the introduced model, but we believe that it does not affect the qualitative features of the

calculated solutions and makes reasonable the computing burden: it will be improved in future investigations, where more powerful computing tools will be used. Starting from the meaning of the symbol used in Figure 3 the unit vector $\hat{\mathbf{r}}$ indicates the direction of the vector r and its orthogonal unit vector $\hat{\mathbf{t}}$ (they are needed to determine, respectively, the longitudinal and the shear waves oscillation direction) can be written as:

$$\hat{\mathbf{r}} = \cos\vartheta\hat{\mathbf{e}}_1 + \sin\vartheta\hat{\mathbf{e}}_2 \tag{23}$$

$$\hat{\mathbf{t}} = -\sin\vartheta\hat{\mathbf{e}}_1 + \cos\vartheta\hat{\mathbf{e}}_2 \tag{24}$$

The vector displacement (see e.g. Mancusi et al. [21] for a similar analysis), assuming that the discrete spectrum includes three different frequencies, is the real part of:

$$\bar{\mathbf{u}} = \Sigma_{j=1}^{3}\left[\frac{A_{jl}}{r}\hat{\mathbf{r}}e^{i(\omega_{jl}t-k_{jl}r)} + \frac{A_{js}}{r}\hat{\mathbf{t}}e^{i(\omega_{js}t-k_{js}r)}\right] \tag{25}$$

where

$$\omega_j = \omega_{jl} = \omega_{js} \qquad \text{for } j = 1, 2, 3 \tag{26}$$

$$A_j = A_{jl} = A_{js} \qquad \text{for } j = 1, 2, 3 \tag{27}$$

where (1) ω_{jl} and ω_{js} are the frequencies of the longitudinal (index l) and shear (index s) waves which are equal to each other in the analysed example (26), (2) A_{jl} and A_{js} represented the source of the longitudinal and the shear waves respectively, (3) k_{jl} and k_{js} are the wavenumber of the longitudinal and the shear waves respectively and the ratios between those terms and the frequency ω_j is related to the velocities of the waves (principal and shear waves), as follows

$$k_{jl} = \frac{\omega_j}{v_{wl}} \qquad \text{for } j = 1, 2, 3 \qquad \text{(for the longitudinal waves)} \tag{28}$$

$$k_{js} = \frac{\omega_j}{v_{ws}} \qquad \text{for } j = 1, 2, 3 \qquad \text{(for the shear waves)} \tag{29}$$

It is possible to prove that the velocities are also related to the Lamè constants as follows,

$$v_{wl} = \sqrt{\frac{\lambda + 2\mu}{\rho}} \tag{30}$$

$$v_{ws} = \sqrt{\frac{\mu}{\rho}} \tag{31}$$

Manipulating equations (23) and (24) by means the equation (22), the displacements imposed at the bottom boundary, by the equation (25), are:

$$\bar{u}_1(X_1) = a_{n1}(t)\Sigma_{h=1}^{3}\left[\frac{X_1 - X_{H1}}{r^2}A_h\sin(\omega_h t - k_{hl}r) - \frac{X_{H2}}{r^2}A_h\sin(\omega_h t - k_{hs}r)\right] \tag{32}$$

$$\bar{u}_2(X_1) = a_{n1}(t)\Sigma_{h=1}^{3}\left[\frac{-X_{H2}}{r^2}A_h\sin(\omega_h t - k_{hl}r) - \frac{X_1 - X_{H1}}{r^2}A_h\sin(\omega_h t - k_{hs}r)\right] \tag{33}$$

where we have pre-multiplied the equation (32) and the equation (33) with a_{n1} that is a window function that allow to consider only the signals into a specific time interval. Note that the amplitude of the imposed waves near the lower blue boundary (which is farther from the hypocenter where the waves originate and propagate through the ground) is on the order of millimeters.

Table 2. Waves paramters we used on the simulations. The indices *l* and *s* refer to the longitudinal and shear waves, respectively.

Wave 1	Wave 2	Wave 3
$\omega_1 = 1.571\,\frac{\text{rad}}{\text{s}}$	$\omega_2 = 3.142\,\frac{\text{rad}}{\text{s}}$	$\omega_3 = 15.708\,\frac{\text{rad}}{\text{s}}$
$v_{wl} = 4216.4\,\frac{\text{m}}{\text{s}}$	$v_{wl} = 4216.4\,\frac{\text{m}}{\text{s}}$	$v_{wl} = 4216.4\,\frac{\text{m}}{\text{s}}$
$v_{ws} = 2434.3\,\frac{\text{m}}{\text{s}}$	$v_{ws} = 2434.3\,\frac{\text{m}}{\text{s}}$	$v_{ws} = 2434.3\,\frac{\text{m}}{\text{s}}$
$k_{1l} = 3.726 \cdot 10^{-4}\,\frac{1}{\text{m}}$	$k_{2l} = 7.451 \cdot 10^{-4}\,\frac{1}{\text{m}}$	$k_{3l} = 3.726 \cdot 10^{-3}\,\frac{1}{\text{m}}$
$k_{1s} = 6.453 \cdot 10^{-4}\,\frac{1}{\text{m}}$	$k_{2s} = 7.451 \cdot 10^{-4}\,\frac{1}{\text{m}}$	$k_{3s} = 6.453 \cdot 10^{-3}\,\frac{1}{\text{m}}$
$A_1 = 320\text{m}^2$	$A_2 = 240\text{m}^2$	$A_3 = 160\text{m}^2$

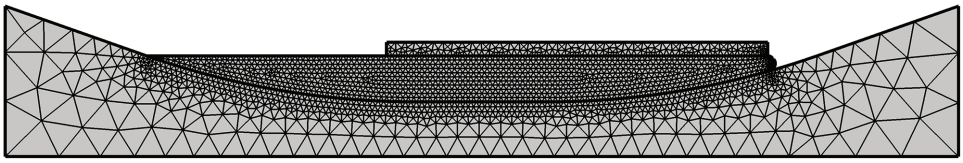

Figure 4. Triangular finite elements.

In Figure 4 the mesh employed is shown. It consists of triangular elements with dimensions not exceeding 469 m in the lower layer (bedrock). Element dimensions. Element dimensions decrease in proximity to the boundary layers, reaching (for the soft layer) maximum dimensions of 40 m.

The three-dimensional Young's moduli Y_s, Y_h, presented in Table 1, are multiplied by an assumed out of plane depth of $d = 1$m to derive the analogous quantities for the bi-dimensional domain, $Y_s^{2D} = Y_s d$ and $Y_h^{2D} = Y_h d$. Then, the Lamè coefficients employed in equation (4) for both the softer and harder layers are determined by equation (21), under the following assumptions:

$$Y = Y_s^{2D}, \quad \nu = \nu_s \qquad \text{for the softer layer} \tag{34}$$

$$Y = Y_h^{2D}, \quad \nu = \nu_h \qquad \text{for the harder layers} \tag{35}$$

Also the mass densities ρ_s and ρ_h are multiplied for the same assumed out of plane depth $d = 1$m to yield the density for the two-dimensional domain under investigation to insert into the equation (5) under the following assumption:

$$\rho = \rho_s^{2D} \qquad \text{for the softer layer} \tag{36}$$

$$\rho = \rho_h^{2D} \qquad \text{for the harder layers} \tag{37}$$

The waves' parameters are shown in Table 2

3.3. Description of the COMSOL code

The analysis described in this work was conducted using COMSOL, a multiphysics finite element software; using this software we were able to carry out a more refined analysis with respect that one by Luca et al. [33]. The model has 30456 degrees of freedom and 3690 triangular elements, into which it has been divided. The size of the elements varies depending on the area of the model: it is reduced near the boundary sharing two subregion with different stiffnesses. The used shape functions are Lagrangian of quadratic order. The implicit methods are more complicated than the explicit ones, in which it is possible to find the solution at the next step by means the only that at the current step, because it is necessary to

solve an equation for each time step that depend for both the states of the system (the current one and the next one). So, mathematically, if $s(t)$ is the state of the system at the current time t and $s(t+\Delta t)$ is the state of the system at the later instant $t+\Delta t$, one has:

$$\begin{aligned} s(t+\Delta t) &= F(s(t)) \qquad \text{for the explicit methods} \\ H(s(t), s(t+\Delta t)) &= 0 \qquad \text{for the implicit methods} \end{aligned} \tag{38}$$

The solver we used for calculate the results is based on the implicit method called *generalized-α* method. Those methods are similar to the second-order BDF (backward differentiation formulas) solver, also based on an implicit method. Unlike this latter method, the generalized-α is a method that allows to control better the degree of damping of high frequencies in the solution and it is more accurate. So that if a solution with sharp gradients is expected, one does not get a very smooth solution due to the damping in the backward method. It is worth to note that, for those same reasons it is also less stable. We used an dynamic load characterised by a discrete spectrum and a time step $t = (800Hz)^{-1}$.

4. Analysis of results

In this section, the comparison between the deformation and the kinetic energy fields and the horizontal and vertical components of the acceleration vector, for the linear and non-linear cases, is shown to emphasize how the non-linear contribution should be taken into consideration when a seismic analysis is carried out. As it is shown in the following subsections the differences, in suitable relative terms, are very large. In the following the superscript *nl* indicates that the corresponding quantity is calculated with the non-linear finite strain tensor $\mathbb{G}$, the third quantity in equation (1) and with the general non-linear evolution equations. Moreover, the superscript *l* indicates that the corresponding quantity is calculated with the linearised version of the strain tensor: i.e. equation (10) and with the linearised evolution equations. Hence, the deformation energies for non-linear and linear cases are denoted as follows,

$$\mathcal{W}^{nl} \qquad \text{for the non-linear case} \tag{39}$$

$$\mathcal{W}^{l} \qquad \text{for the linear case} \tag{40}$$

In the same way, the kinetic energies for non-linear and linear cases are denoted as follows,

$$\mathcal{K}^{nl} \qquad \text{for the non-linear case} \tag{41}$$

$$\mathcal{K}^{l} \qquad \text{for the linear case} \tag{42}$$

Hence, the relative non-linear/linear energies are calculated in the following way:

$$\tilde{\mathcal{W}} = \frac{\mathcal{W}^{nl} - \mathcal{W}^{l}}{\bar{\mathcal{W}}^{l}} \tag{43}$$

$$\tilde{\mathcal{K}} = \frac{\mathcal{K}^{nl} - \mathcal{K}^{l}}{\bar{\mathcal{K}}^{l}} \tag{44}$$

where the symbols $\bar{\mathcal{W}}^{l}$ and $\bar{\mathcal{K}}^{l}$ represent the average, on the domain, of the linear deformation and kinetic energy respectively. The accelerations (and their difference between the non-linear and linear case) are normalized by the gravity acceleration g. Taking into account that the displacements are denoted as u_i for the linear case and as v_i for the non-linear case, the horizontal and vertical accelerations for each point for the linear and for the non-linear cases are denoted, respectively, as follows,

$$\tilde{\ddot{u}}_i = \frac{\ddot{u}_i}{g} \qquad \text{for the linear case} \tag{45}$$

$$\tilde{\ddot{v}}_i = \frac{\ddot{v}_i}{g} \qquad \text{for the non-linear case} \tag{46}$$

and the comparison has been obtained by the difference:

$$\tilde{a}_i = \tilde{\ddot{v}}_i - \tilde{\ddot{u}}_i \tag{47}$$

Clearly the index i takes on values equal to 1 (horizontal acceleration) or 2 (vertical acceleration).

4.1. Comparison of the deformation energy fields in linear and non-linear cases and formation of energy difference boundary layers

The deformation energy represents an important measure of the deformations during the seismic action that it is worth to be investigated. In the Figure 5, it is shown the highest (or lowest) amount of the percentage difference $\tilde{\mathcal{W}}$, in the equation (43), reached on the domain for each time instant.

Note that some extreme values are due clearly to numerical errors that are concentrated only in isolated elements. In Figure 5, the lines corresponding to $y = \pm 1$ are highlighted to show how large are the relative errors between the two methods (clearly the value 1 means differences equal to 100%). Future numerical simulations, with more powerful computing tools, will eliminate these spurious values by using finer finite elements and regularization techniques, such as higher gradient models, which are better suited for discontinuous stiffness fields. To mitigate the impact of the aforementioned numerical errors [119], the color legend in the following contour plots is restricted to the range [–1, 1]. However, for some plots (e.g., Figure 6(b)), a different range might seem more appropriate. These choices were made to improve the readability of the plots when the actual range of values is too small to be effectively represented within the wider range [–1, 1]. The contour plots of the deformation energy in the non-linear case $\mathcal{W}^{nl}$ and its comparison $\tilde{\mathcal{W}}$ with respect the linear one are shown for some time instants in Figure 6–9. In the Figure 5(a) (and clearer in Figure 5(b)) notice that, already during the first seconds when the seismic action excites the ground, the relative difference $\tilde{\mathcal{W}}$ is not negligible (having value much higher then 100%).

Note that from the very beginning, the (albeit small) differences are concentrated at the material transition, from the bedrock to the softer intermediate layer. In addiction, the deformation energy (at the Figure 6(a) and (b) appears almost uniform, and it is the result of the composition of several spherical waves with different velocities and wave lengths. Despite that some differences are present close to the boundary layer as it is shown in Figure 6(c).

It has to be observed that from the beginning of the simulation, the relative difference is substantial (Figure 7(c)) with an extensive region where the difference $\tilde{\mathcal{W}}$ exceeds 20% warrants attention.

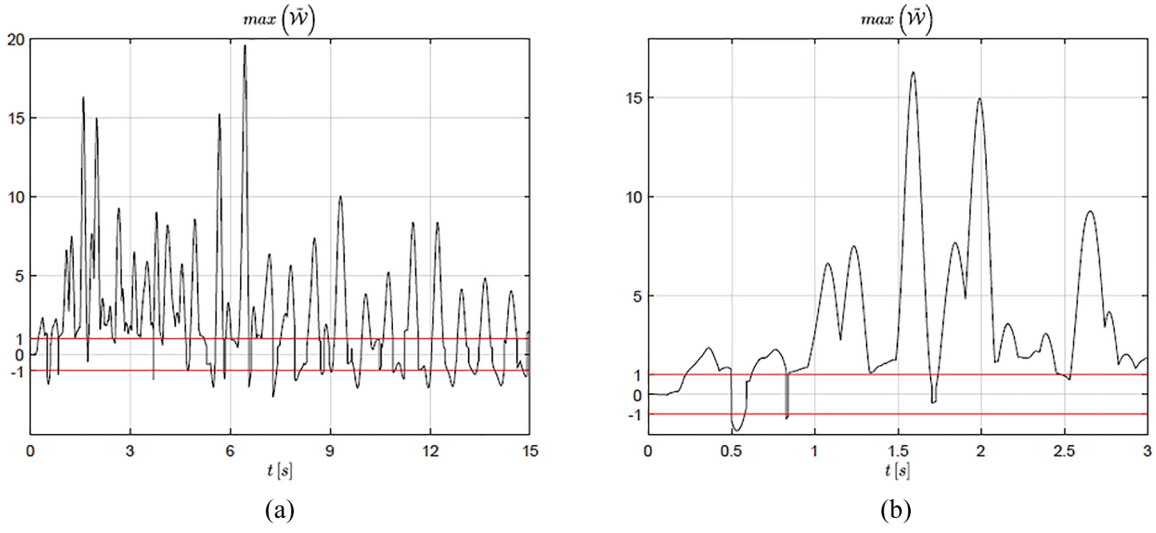

Figure 5. Maximum value of $\tilde{\mathcal{W}}$, defined in equation (43), for (a) the whole analyses and (b) a zooming of the first 3 seconds.

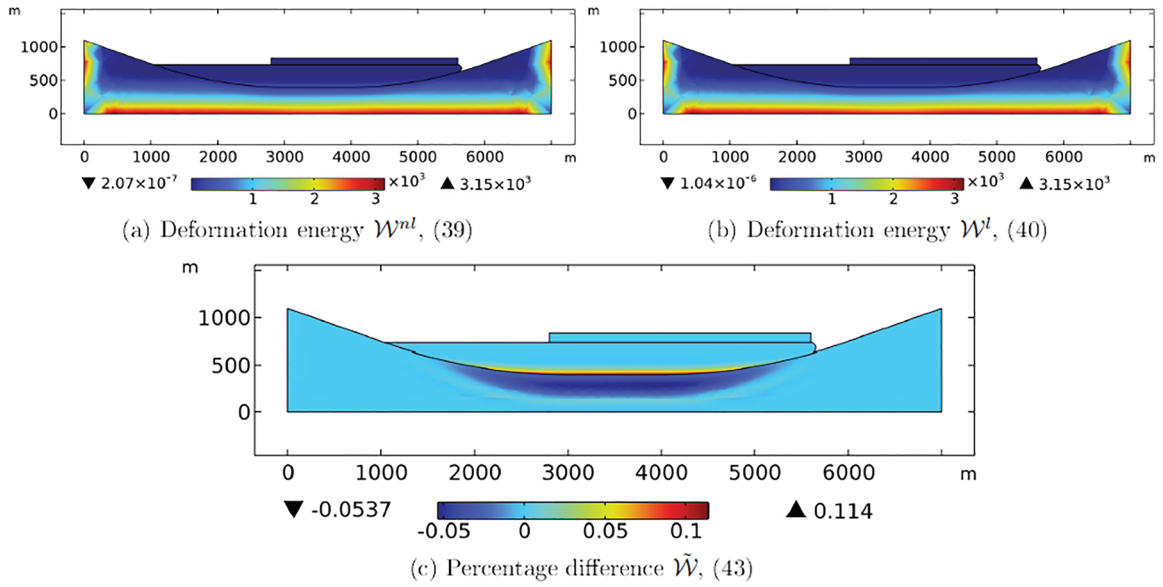

Figure 6. Deformation energy calculated using (a) a non-linear approach, $\mathcal{W}^{nl}$ (Pa), (b) a linear approach, $\mathcal{W}^{l}$ (Pa), and (c) the percentage difference, $\tilde{\mathcal{W}}$, between the non-linear and linear cases at $t = 0.15$s.

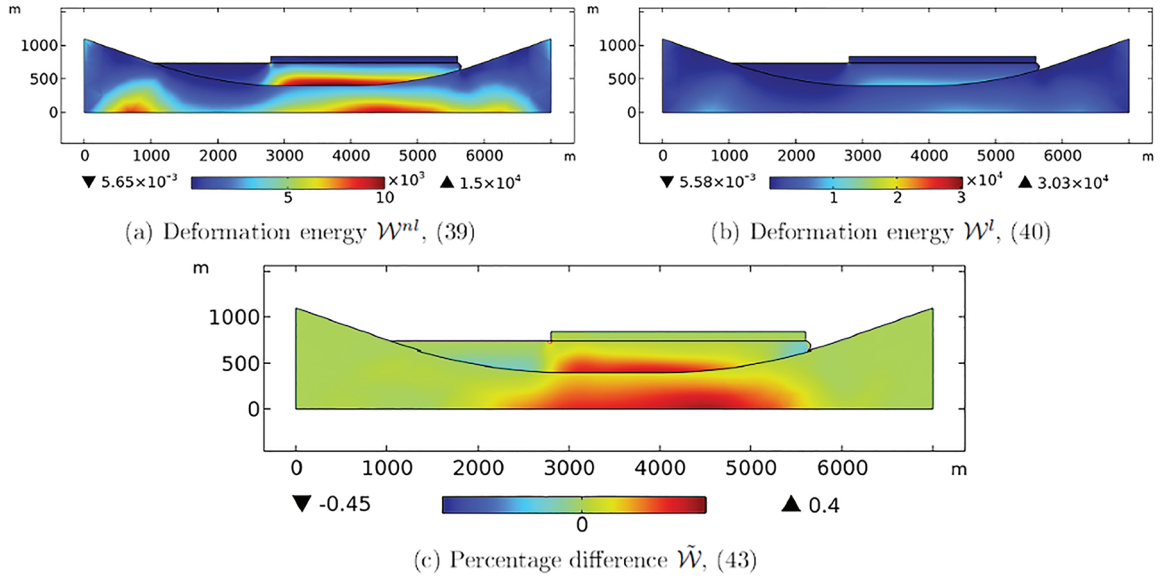

Figure 7. Deformation energy calculated using (a) a non-linear approach, $\mathcal{W}^{nl}$ (Pa), (b) a linear approach, $\mathcal{W}^{l}$ (Pa), and (c) the percentage difference, $\tilde{\mathcal{W}}$, between the non-linear and linear cases at $t = 0.5$s.

Figure 8(c) reveals significantly larger differences. Notably, even after excluding the extreme values, the energy relative difference exceeds 100% close to the boundary layer.

The whole evolution in time of the difference $\tilde{\mathcal{W}}$ with respect the linear case (43), is shown in a video, which is included in the form of supplementary materials.

4.2. Comparison of the kinetic energy fields in linear and non-linear cases and the formation of energy difference boundary layers

Kinetic energy fields serve as key indicators of velocities within a system under consideration and deserve thorough investigation. Following Section 4.1, the highest (or lowest) value of the difference of the kinetic energy, denoted by $\tilde{\mathcal{K}}$ and defined in equation (44), reached in the domain for each instant of time is shown

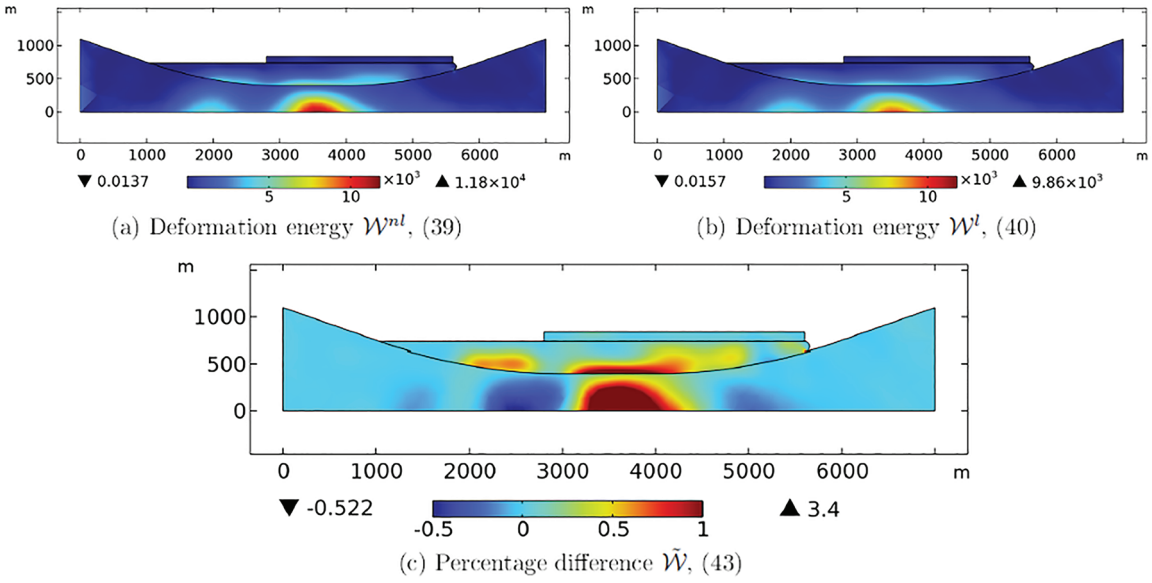

Figure 8. Deformation energy calculated using (a) a non-linear approach, $\mathcal{W}^{nl}$ (Pa), (b) a linear approach, $\mathcal{W}^{l}$ (Pa), and (c) the percentage difference, $\tilde{\mathcal{W}}$, between the non-linear and linear cases at $t = 1.5$s.

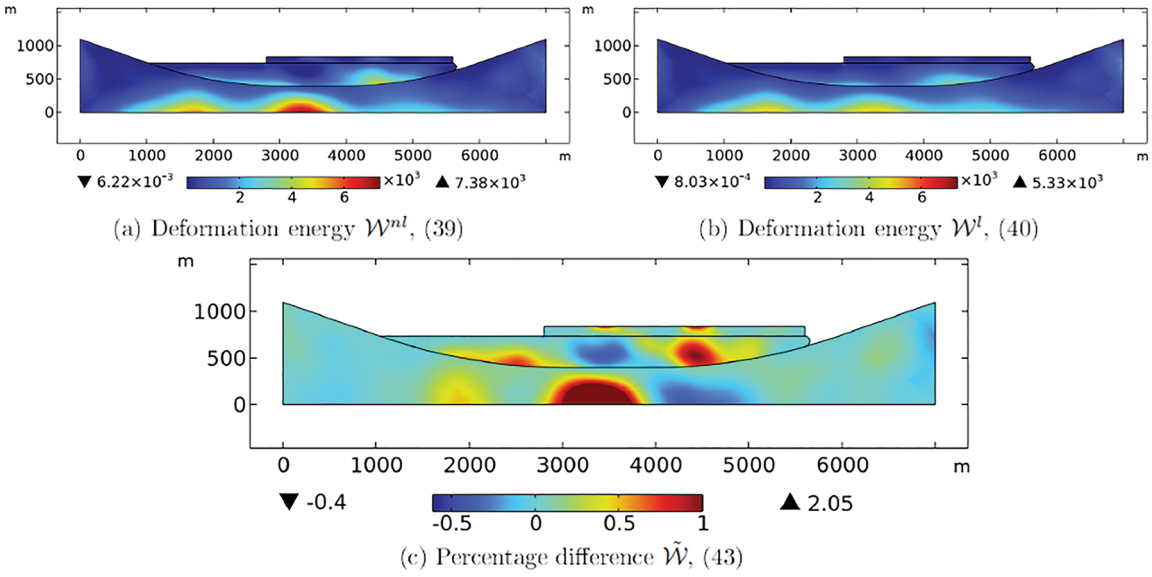

Figure 9. Deformation energy calculated using (a) a non-linear approach, $\mathcal{W}^{nl}$ (Pa), (b) a linear approach, $\mathcal{W}^{l}$ (Pa), and (c) the percentage difference, $\tilde{\mathcal{W}}$, between the non-linear and linear cases at $t = 3$s.

in Figure 10. Then, the contour plots of both the kinetic energy $\mathcal{K}^{nl}$ calculated with our non-linear model and the difference $\tilde{\mathcal{K}}$ are presented in Figures 11–14, 15, and 16.

As seen in Figure 11, the two considered models, linear and non-linear, show a remarkable difference near the boundary where the transition from an harder to a softer layer occurs, i.e., where strong material inhomogeneity occurs. It is worth noting that, just as in the Section 4.1, also for the kinetic energy we focus on the first 3 seconds, i.e., in the time interval when the seismic waves acts on the domain. As one can see, the difference continues to be not negligible also after the third second.

Figures 11(c) and 12(c) reveal that the largest differences in kinetic energy are initially concentrated near the boundary between the bedrock and the softer layer. Subsequently, these differences propagate

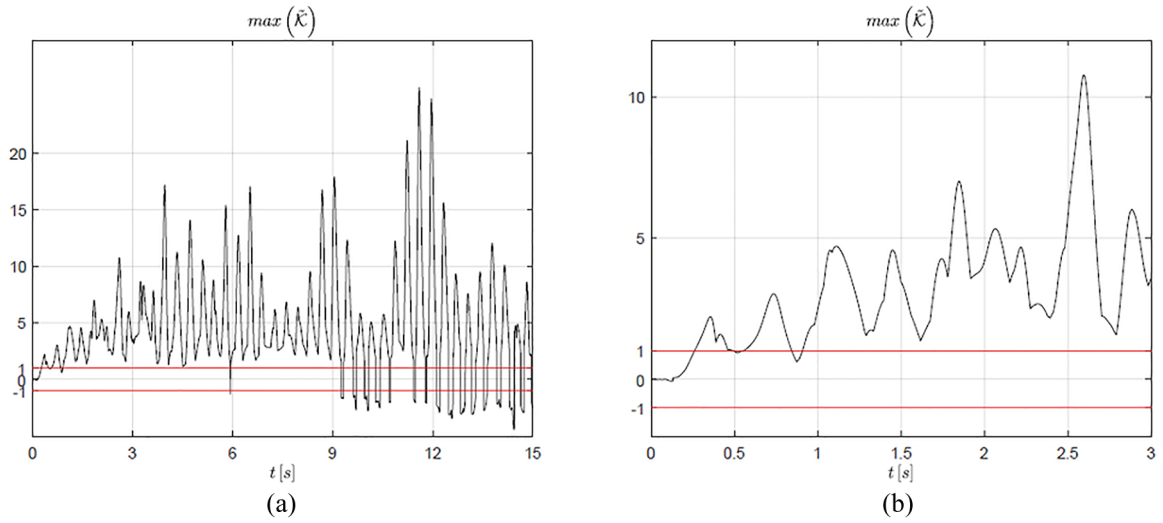

Figure 10. Maximum value of differences $\tilde{\mathcal{K}}$ with respect the time between the two cases (linear and non-linear) for (a) the whole time interval of the performed analyses and (b) a zooming of the first 3 seconds.

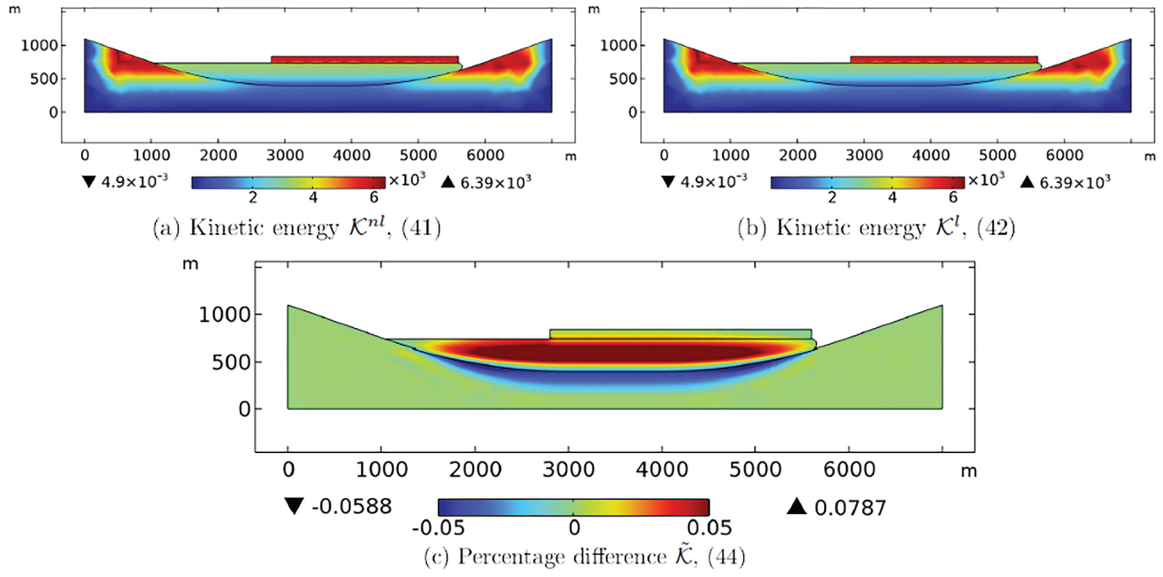

Figure 11. Kinetic energy calculated using (a) a non-linear approach, $\mathcal{K}^{nl}$ (Pa), (b) a linear approach, $\mathcal{K}^{l}$ (Pa), and (c) the percentage difference, $\tilde{\mathcal{K}}$, between the non-linear and linear cases at $t = 0.15$s.

through the softer material towards the rigid top layer. Notably, even during the initial stages of ground excitation by the seismic action, the relative difference is substantial. For example, Figure 12(c) shows that the difference between the non-linear and linear analyses can exceed 100%.

During the first fractions of second, period in which the seismic wave acts on the considered propagation region (remember that the seismic action goes on for 3 s) the higher differences are concentrated at the top of the propagation region, and exactly where the stiffness changes and a material non-linearity is activated. The difference propagates from the harder layer, at the top, to the softer one and vice versa because the reflection of the seismic wave (Figures 12(c) and 13(c)).

During the seismic excitation significant differences between linear and non-linear models are calculated. For example at $t = 2$ s (in Figure 14), it can observe that the main differences are mostly concentrated in the top harder layer, and its value increases noticeably reaching very relevant values as it is shown, for example, in Figure 14(c).

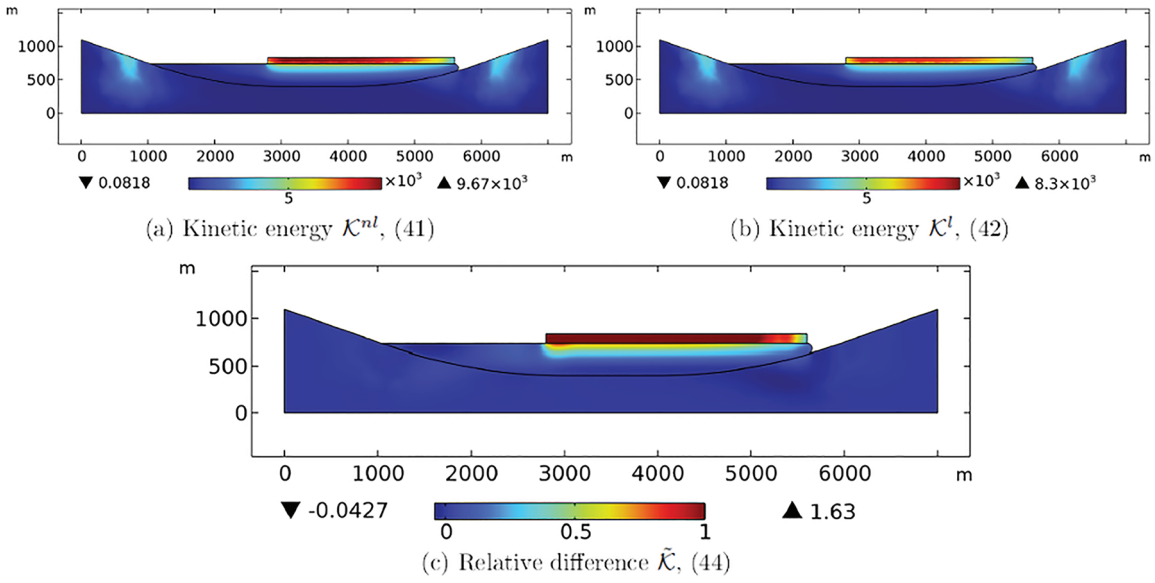

Figure 12. Kinetic energy calculated using (a) a non-linear approach, $\mathcal{K}^{nl}$ (Pa), (b) a linear approach, $\mathcal{K}^{l}$ (Pa), and (c) the percentage difference, $\tilde{\mathcal{K}}$, between the non-linear and linear cases at $t = 0.3$s.

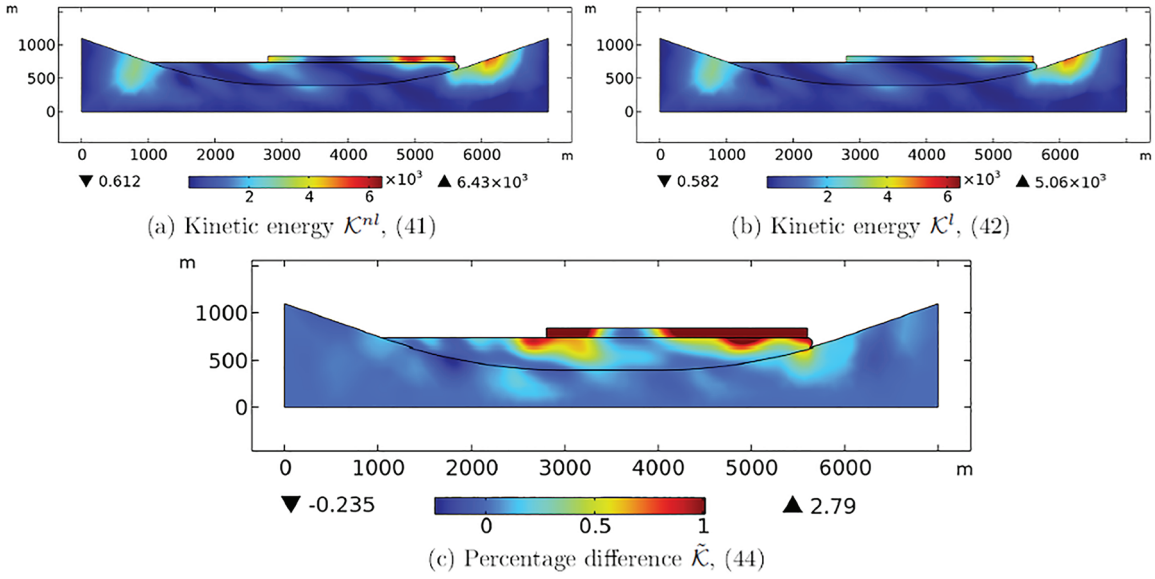

Figure 13. Kinetic energy calculated using (a) a non-linear approach, $\mathcal{K}^{nl}$ (Pa), (b) a linear approach, $\mathcal{K}^{l}$ (Pa), and (c) the percentage difference, $\tilde{\mathcal{K}}$, between the non-linear and linear cases at $t = 1$s.

In Figure 10(b), a big peak of relative difference is clearly evident. To avoid commenting on values that may be due to numerical errors, the contour plot in the neighboring of that instant of time (specifically at $t = 2.6$ s), is shown in Figure 15. At this instant, the value of the difference is very high. Moreover, on the harder top layer a region is clearly visible where the kinetic energy reaches a high value. This makes the difference $\tilde{\mathcal{K}}$ (see the Figure 15(c)) absolutely non-negligible.

At the instant $t = 3$ s (Figure 16), when the seismic excitation ends, its effects continue to be relevant in the region where the wave propagation is studied.

Also after the instant $t = 3$, the differences between the predictions of non-linear and linear models increase significantly as shown in Figure 10(a). This implies that the kinetic energy (and therefore

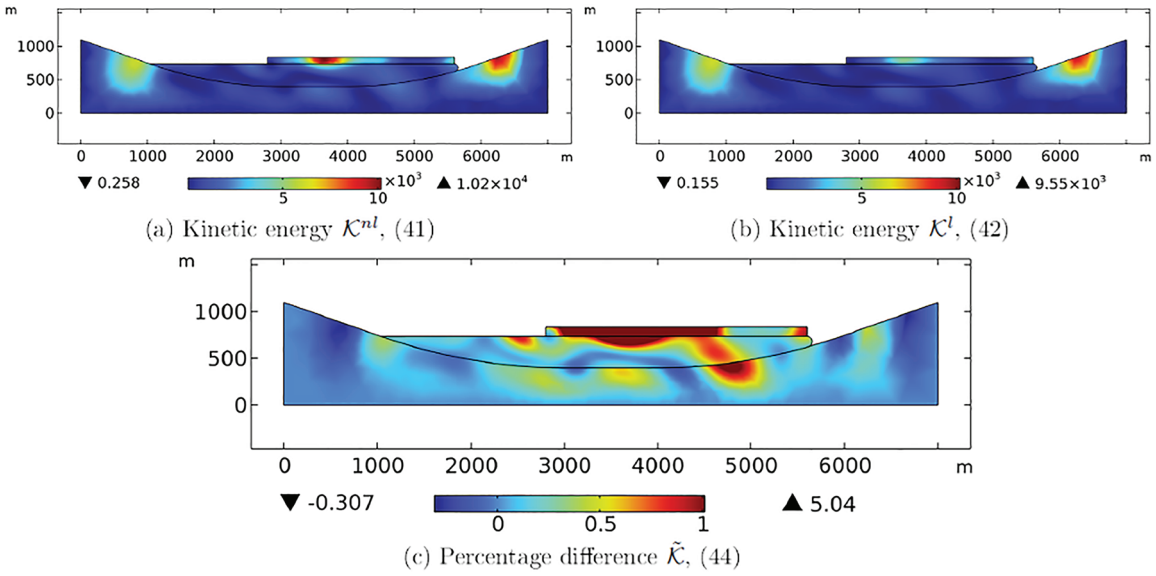

Figure 14. Kinetic energy calculated using (a) a non-linear approach, $\mathcal{K}^{nl}$ (Pa), (b) a linear approach, $\mathcal{K}^{l}$ (Pa), and (c) the percentage difference, $\tilde{\mathcal{K}}$, between the non-linear and linear cases at $t = 2$s.

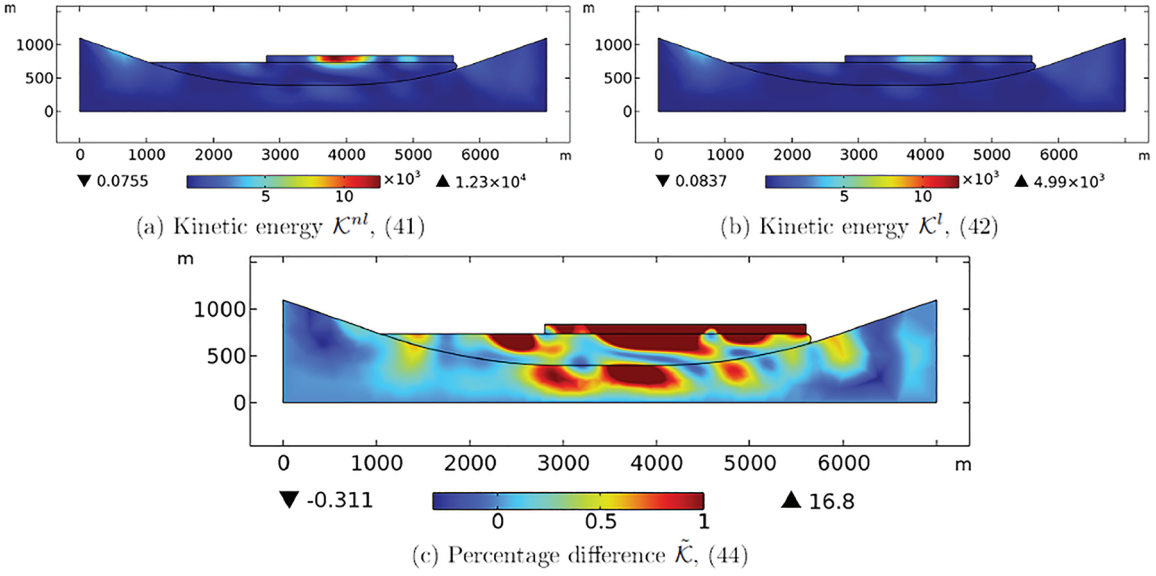

Figure 15. Kinetic energy calculated using (a) a non-linear approach, $\mathcal{K}^{nl}$ (Pa), (b) a linear approach, $\mathcal{K}^{l}$ (Pa), and (c) the percentage difference, $\tilde{\mathcal{K}}$, between the non-linear and linear cases at $t = 2.6$s.

the velocities of each material point) calculated by means of a linear model does not seem to give reliable predictions. It is clear that such differences cannot be overlooked and that more careful modelling assumptions are required. The whole evolution in time of the relative difference $\tilde{\mathcal{K}}$ with respect to the kinetic energy calculated using the non-linear and the linear model (44), is shown with a video included in the form of supplementary materials.

4.3. Comparison of acceleration fields

The accelerations (45) and (46) (either horizontal and vertical) in certain points have been calculated and their differences (47) (between the non-linear and linear models) are seen to be substantial. These results indicate a need to reconsider the current approaches used to predict seismic phenomena. The Figure 17

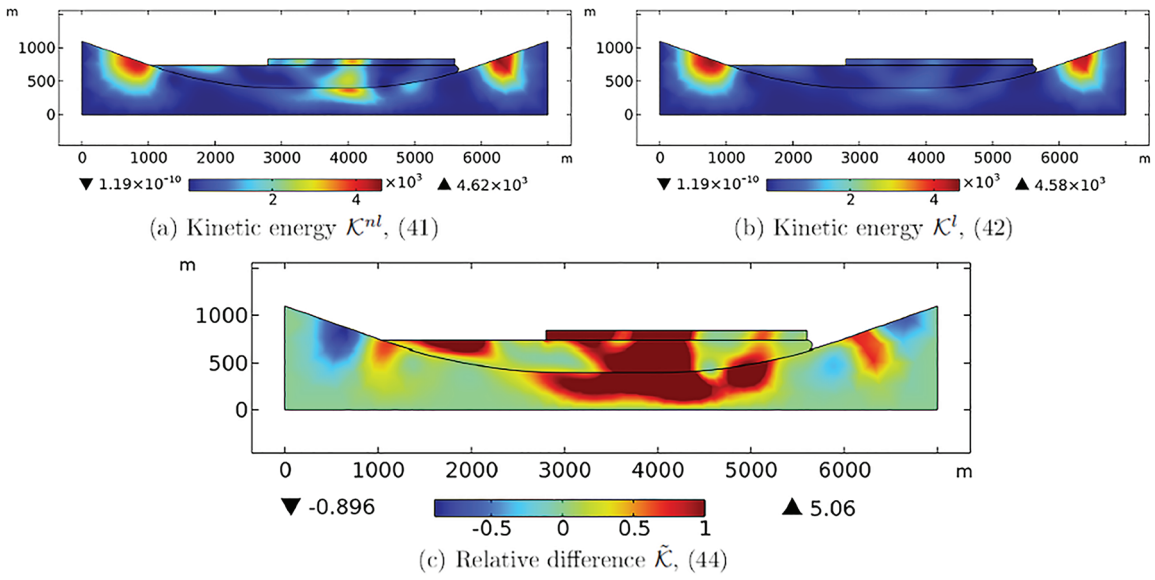

Figure 16. Kinetic energy calculated using (a) a non-linear approach, $\mathcal{K}^{nl}$ (Pa), (b) a linear approach, $\mathcal{K}^{l}$ (Pa), and (c) the percentage difference, $\tilde{\mathcal{K}}$, between the non-linear and linear cases at $t = 3$s.

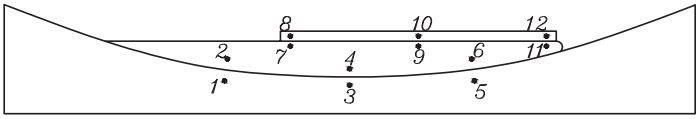

Figure 17. Analyzed points.

shows the points which we have chosen, on the basis of the evidence gathered by Luca et al. [33], in order to compare the predictions of linear and non-linear models: recall that the accelerations difference used for getting the presented comparisons is defined in equation (47).

The first 6 point are chosen near the boundary between the bedrock layer and the softer one, while the next 6 ones are taken close to the boundary between the softer and the top rigid layer. Either the horizontal and vertical accelerations ($\tilde{\ddot{u}}_i$ and $\tilde{\ddot{v}}_i$ respectively for the linear and non-linear cases) and the difference $\tilde{a}_i$ (calculated as in equations (45)–(47)) are plotted in Figures 18–29 for all the points defined in Figure 17. The figures below (namely 18–29) are structured with the following scheme:

- On the left hand side the evolution in time of the accelerations, defined as in equations (45) and (46) and scaled by the gravity acceleration g, of the considered point (for the linear $\tilde{\ddot{u}}_i$ and non-linear $\tilde{\ddot{v}}_i$ case) are shown for each direction (i.e. for $i = 1, 2$).
- On the right hand side the differences $\tilde{a}_i$, denoted as in equation (47), are shown. Notably, these differences are plotted as a fraction of the gravitational acceleration g.

In Figures 18–23, the accelerations of the points close to the boundary between the bedrock and the softer layer are shown.

In Figures 18 and 19, the first couple of points are considered (Point 1 and Point 2). Although, for this couple of points, the differences $\tilde{a}_i$ in equation (47) do not reach their highest values, they are also higher than $0.2g$ which corresponds to an approximate difference of $2\frac{\mathrm{m}}{\mathrm{s}^2}$.

Analyzing the couple of point that follows (i.e. Point 3 (Figure 20) and 4 (Figure 21)), the difference increases by a substantial amount (see the differences of the vertical accelerations), reaching the important value of about $0.7g$. Those clearly are quantities that must warn the modellers and all those whose decisions depend on their predictions.

At the upper boundary, between the softer layer and the harder block, on which the downtown of L'Aquila is located, the values of the differences continue to be very high, having values higher than

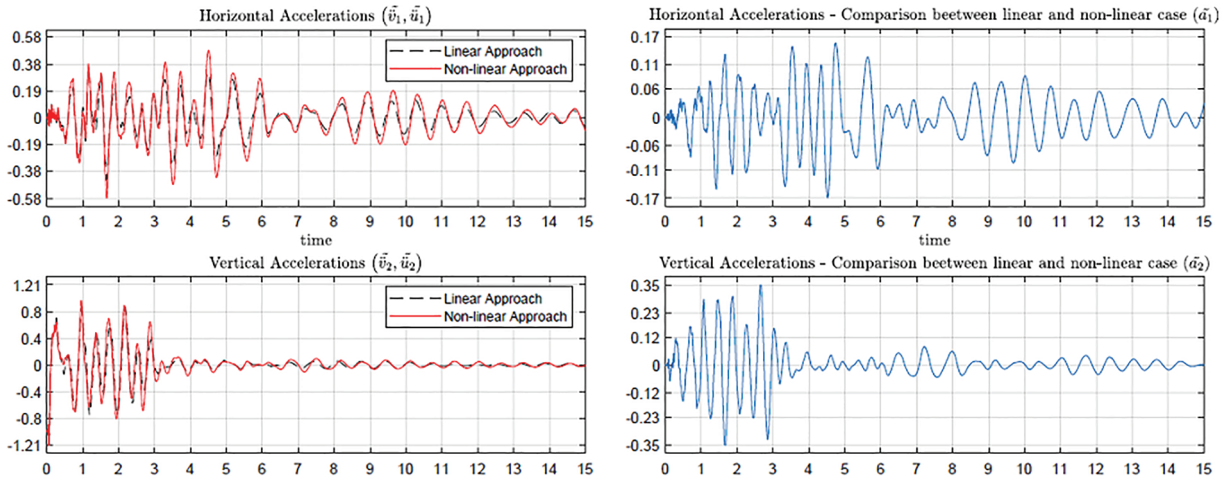

Figure 18. Comparison of the horizontal and vertical accelerations, between the non-linear $\tilde{v}_i$ and linear $\tilde{u}_i$ cases (pictures on the left) and their differences $\tilde{a}_i$ (pictures on the right), gotten by the equations (45)–(47) for the Point 1.

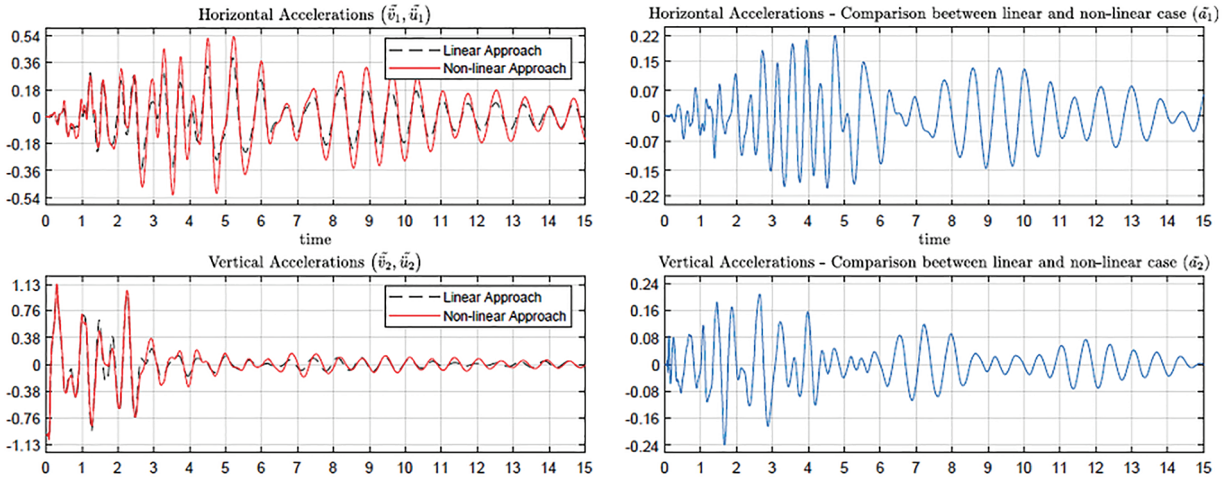

Figure 19. Comparison of the horizontal and vertical accelerations, between the non-linear $\tilde{v}_i$ and linear $\tilde{u}_i$ case, (pictures on the left) and their differences $\tilde{a}_i$ (picture on the right) gotten by the equations (45)–(47) for the Point 2.

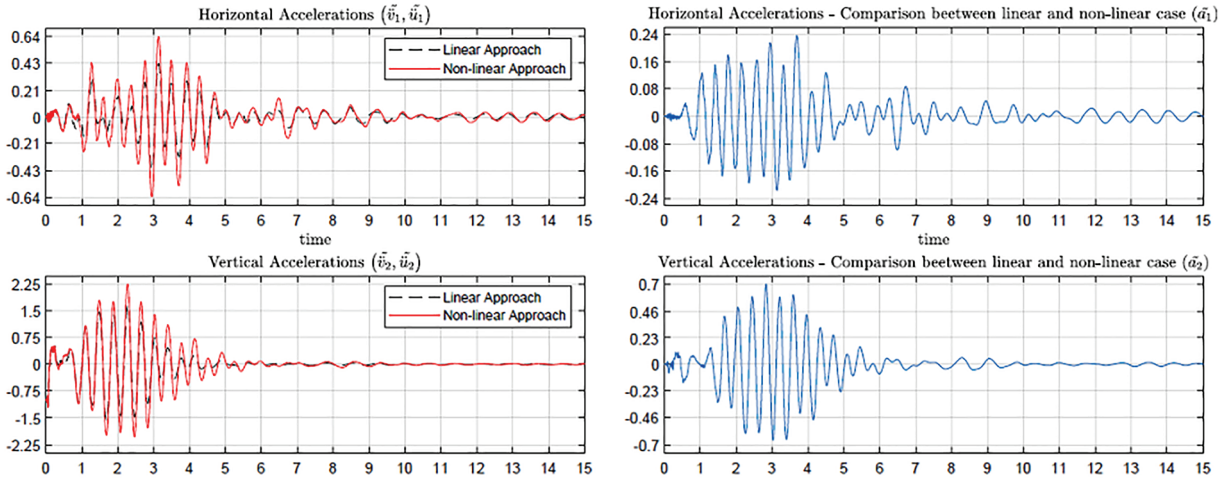

Figure 20. Comparison of the horizontal and vertical accelerations, between the non-linear $\tilde{v}_i$ and linear $\tilde{u}_i$ case, (pictures on the left) and their differences $\tilde{a}_i$ (picture on the right) gotten by the equations (45)–(47) for the Point 3.

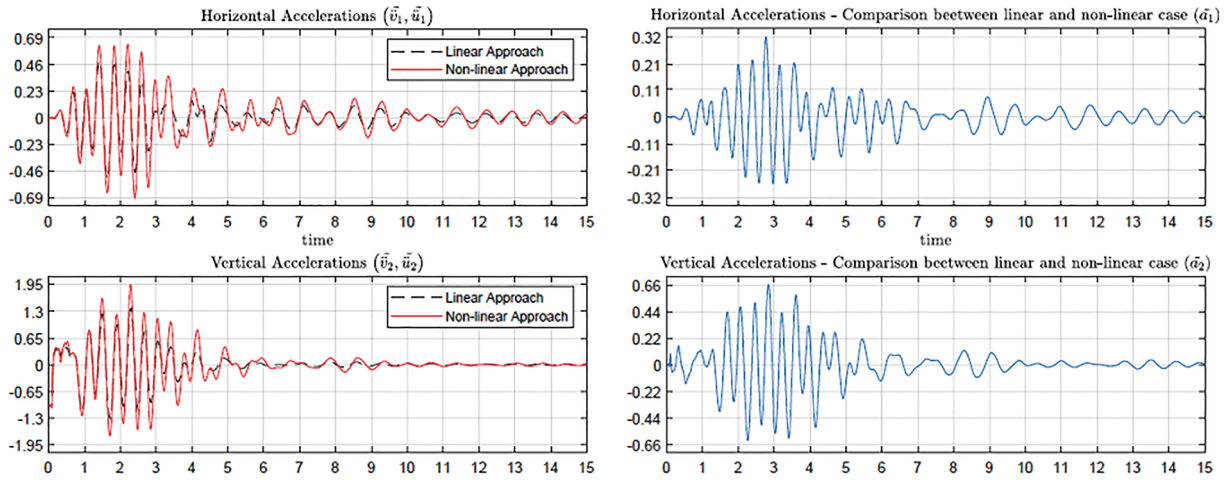

Figure 21. Comparison of the horizontal and vertical accelerations, between the non-linear $\ddot{\tilde{v}}_i$ and linear $\ddot{\tilde{u}}_i$ case, (pictures on the left) and their differences $\tilde{a}_i$ (picture on the right) gotten by the equations (45)–(47) for the Point 4.

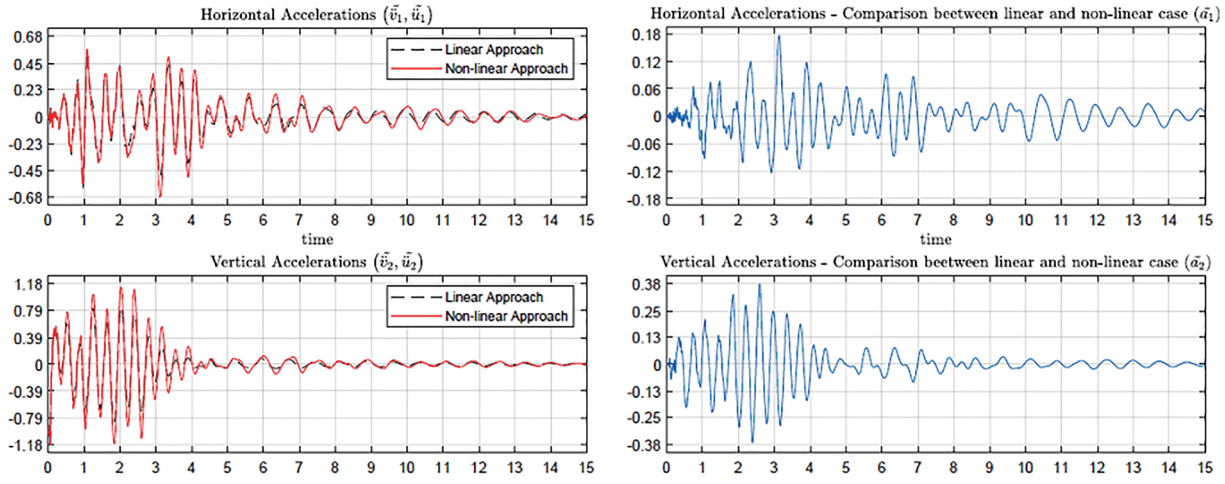

Figure 22. Comparison of the horizontal and vertical accelerations, between the non-linear $\ddot{\tilde{v}}_i$ and linear $\ddot{\tilde{u}}_i$ case, (pictures on the left) and their differences $\tilde{a}_i$ (picture on the right) gotten by the equations (45)–(47) for the Point 5.

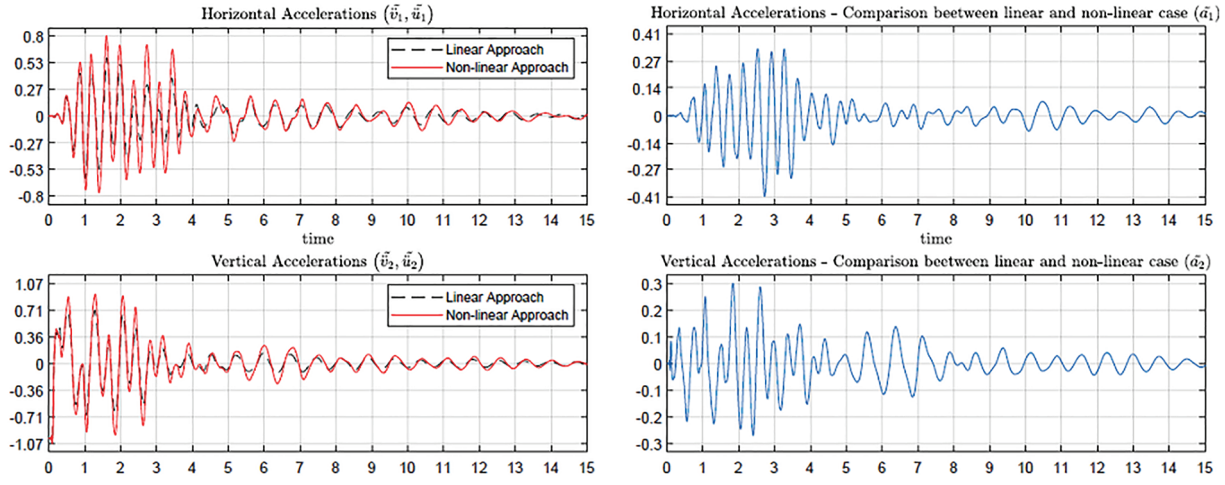

Figure 23. Comparison of the horizontal and vertical accelerations, between the non-linear $\ddot{\tilde{v}}_i$ and linear $\ddot{\tilde{u}}_i$ case, (pictures on the left) and their differences $\tilde{a}_i$ (picture on the right) gotten by the equations (45)–(47) for the Point 6.

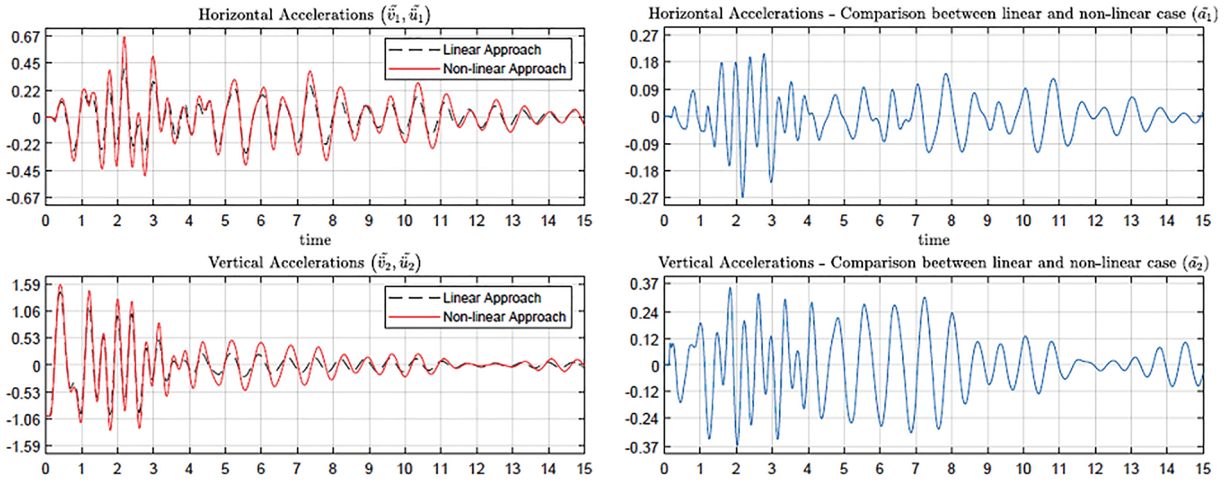

Figure 24. Comparison of the horizontal and vertical accelerations, between the non-linear $\tilde{\tilde{v}}_i$ and linear $\tilde{\tilde{u}}_i$ case, (pictures on the left) and their differences $\tilde{a}_i$ (picture on the right) gotten by the equations (45)–(47) for the Point 7.

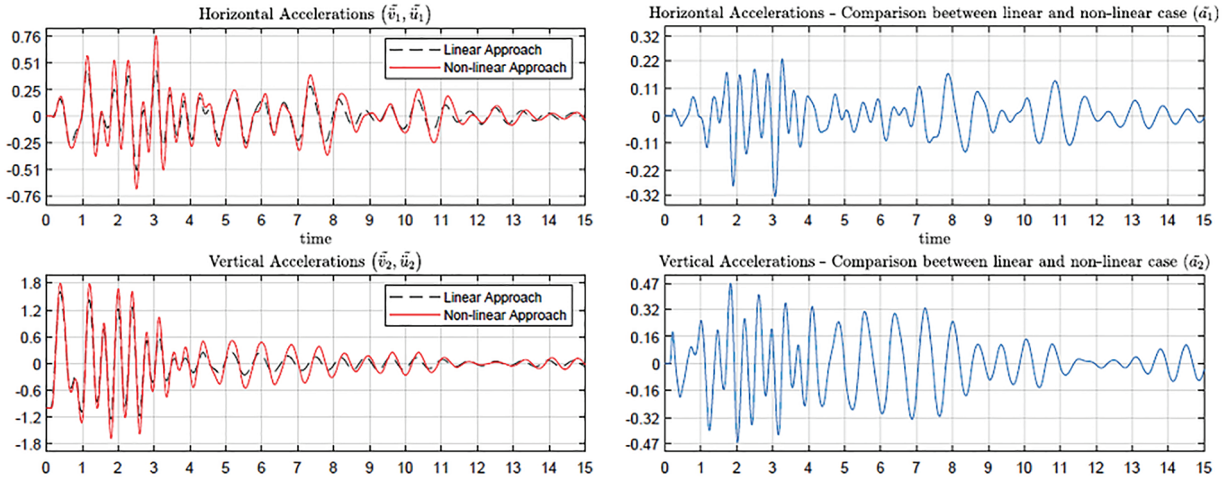

Figure 25. Comparison of the horizontal and vertical accelerations, ween the non-linear $\tilde{\tilde{v}}_i$ and linear $\tilde{\tilde{u}}_i$ case, (pictures on the left) and their differences $\tilde{a}_i$ (picture on the right) gotten by the equations (45)–(47) for the Point 8.

20% of g and, in same case, reaching error around 70% of g (as in the Figures 27 and 29). In the following figures, these strongly high values of the errors are shown.

The observed substantial discrepancies in the acceleration field impose a paradigm change in the choices to be accepted when modelling seismic wave propagation. The non-linear phenomena require a careful consideration due to their proven potential for significant impact. This emphasis is particularly relevant in the light of the findings presented in this work: moreover, by now, modern theoretical and numerical tools allow for the development of predictive analyses based on sophisticated non-linear models.

5. Conclusion

The results of the numerical simulations presented in this work demonstrate that the thesis on which we have based our investigation is correct: linear continuous models are not suitable to describe the effects at ground of large energy earthquakes (Magnitude larger than 6 Mw), in particular when the superficial

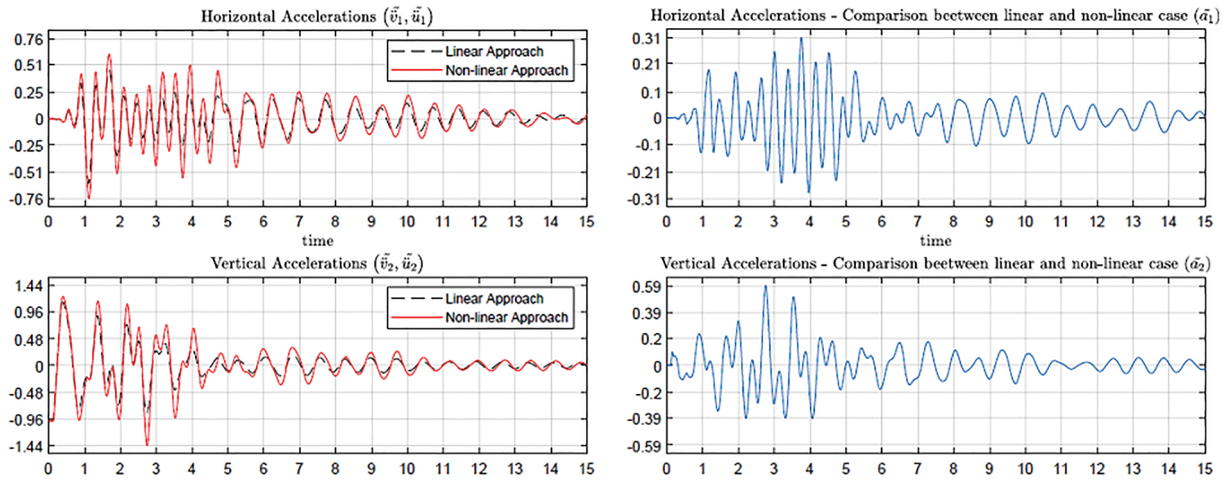

Figure 26. Comparison of the horizontal and vertical accelerations, between the non-linear $\ddot{\tilde{v}}_i$ and linear $\ddot{\tilde{u}}_i$ case, (pictures on the left) and their differences $\tilde{a}_i$ (picture on the right) gotten by the equationsss (45)–(47) for the Point 9.

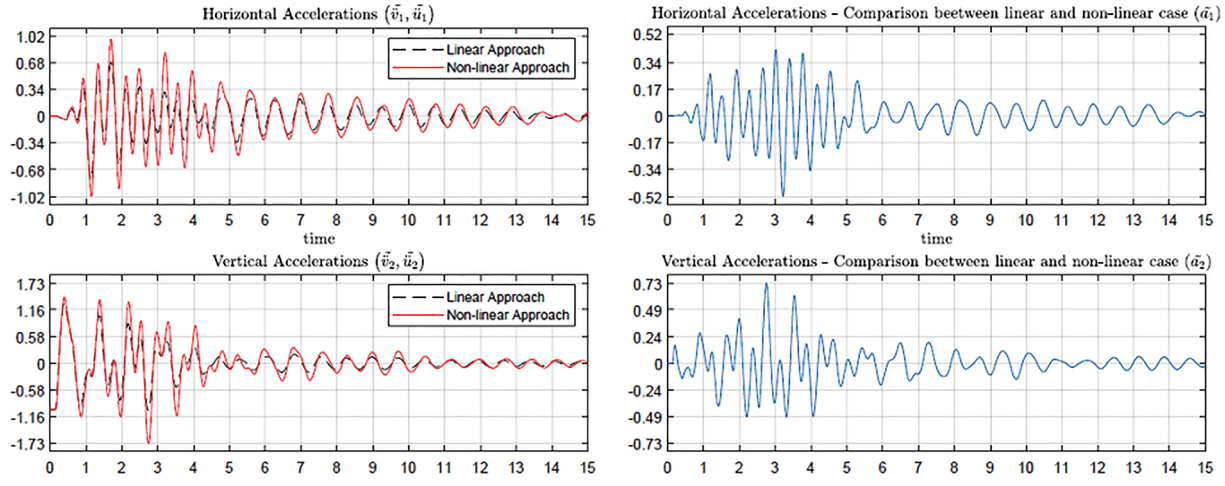

Figure 27. Comparison of the horizontal and vertical accelerations, between the non-linear $\ddot{\tilde{v}}_i$ and linear $\ddot{\tilde{u}}_i$ case, (pictures on the left) and their differences $\tilde{a}_i$ (picture on the right) gotten by the (45)–(47) for the Point 10.

crust is constituted by inhomogeneous materials. We therefore claim that it is worth considering non-linearities when conducting the analysis of seismic effects on structures and infrastructures. As it shown at the section 4 large differences in the predicted values of deformations, velocities, and accelerations are found when using linear or non-linear models. Moreover, using the non-linear inhomogeneous model presented here we can predict where the highest values of accelerations must be expected, and therefore we believe to have supplied an important guide to future experimental and surveying activities. Moreover the supplied predictions could change the seismic hazard evaluation, to be incorporated in the design prescriptions. Aforementioned differences can make the linear seismic study useless, as not only the predicted values of most relevant quantities are quantitatively different, but also the qualitative features of predicted phenomena may differ drastically. While the preliminary non-linear model presented here requires significant refinement to accurately capture the complexities of the 2009 L'Aquila Earthquake, it demonstrates a superior fit to available experimental data compared to linear models. To further assess the model's capabilities and limitations and to generalize its applicability beyond the specific case of the Aterno River Valley and the 2009 L'Aquila earthquake, a systematic comparison with a wider range of well-documented earthquake events will be the focus of future research. This will allow us to evaluate the model's robustness and identify any limitations in its predictive capabilities under various seismic

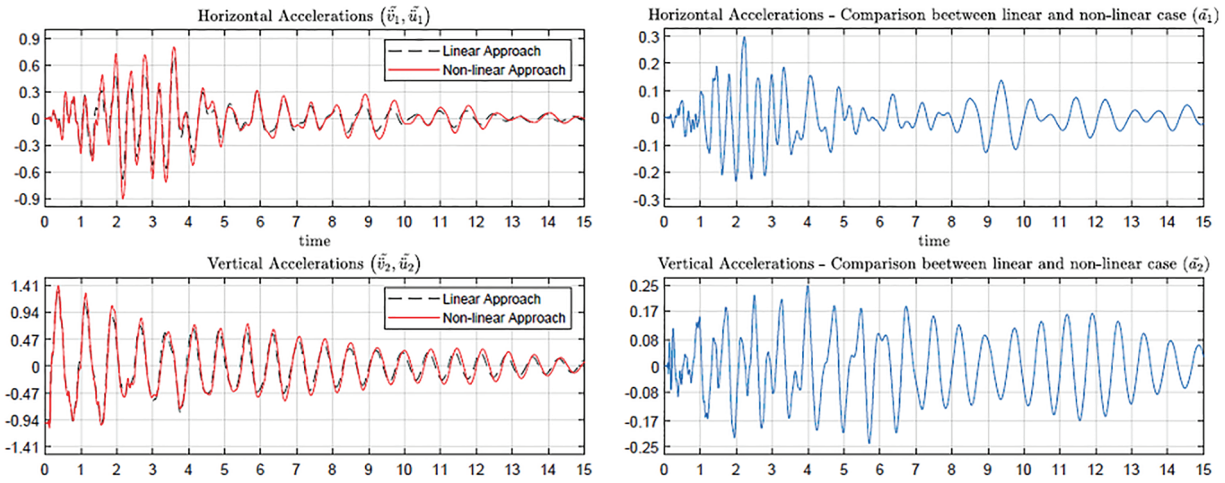

Figure 28. Comparison of the horizontal and vertical accelerations, between the non-linear $\tilde{v}_i$ and linear $\tilde{u}_i$ case, (pictures on the left) and their differences $\tilde{a}_i$ (picture on the right) gotten by the (45)–(47) for the Point 11.

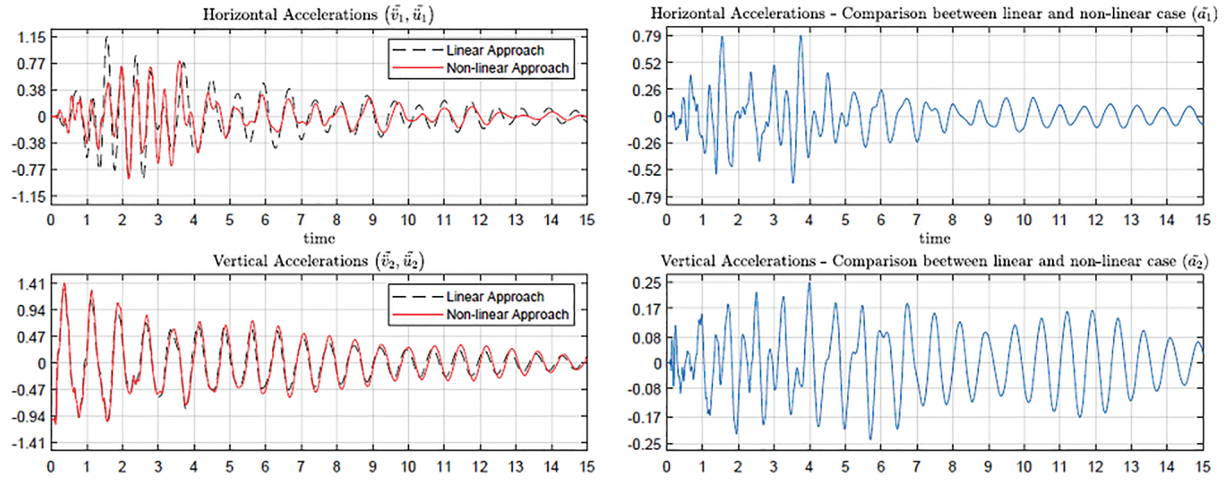

Figure 29. Comparison of the horizontal and vertical accelerations, between the non-linear $\tilde{v}_i$ and linear $\tilde{u}_i$ case, (pictures on the left) and their differences $\tilde{a}_i$ (picture on the right) gotten by the (45)–(47) for the Point 12.

conditions. In particular, we remark that with our 2D geometrically non-linear isotropic model, in which stiffnesses are piecewise constant, we can predict more carefully, both quantitatively and qualitatively, some experimental evidence concerning the measured spectral ratios: while this subject will be carefully described in a future paper, in the present conclusion we will start reporting about preliminary, but very suggestive, results concerning these ratios. This study highlights the significant role of assumptions, such as boundary conditions and material properties, in influencing the accuracy of non-linear models. While acknowledging the potential impact of simplified boundary conditions on the model's ability to replicate experimental data, it is crucial to recognize the complex interplay of various factors governing the behavior of such systems. Geometric non-linearities represent one aspect of this complex interaction, alongside other factors such as material non-linearities (e.g., plasticity, damage, cracking) and more sophisticated boundary conditions. Future investigations will delve deeper into the influence of these additional factors to provide a more comprehensive understanding of the system's behavior. We expect that a predictive modelling for the seismic wave propagation in the Aterno River Valley must include novel and relevant material non-linearity assumptions, considered the proven expected high concentration of deformation energy at the discontinuity interfaces and the present knowledge about the mechanical properties of geomaterials. In fact, only by assuming the simplest geometric non-linearity behaviour, exposed in this work

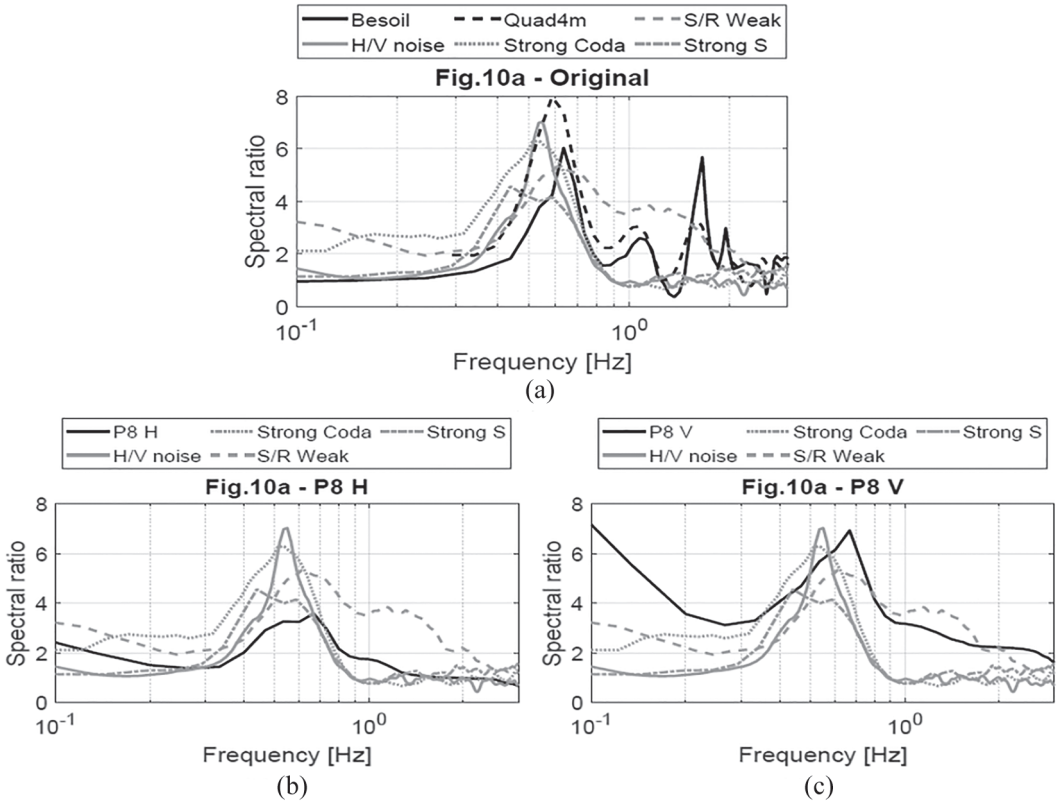

Figure 30. The spectral ratio between the horizontal (b) and vertical (c) non-linear accelerations of the Point 8 and the Point 1 (that is situated into the bedrock, see Figure 17) compared with the Figure 11(a) from Luca et al. [33], shown at the top of the figure (a). The spectral are smoothed with a 50 points moving window.

at the Section 3 (particularly at the Section 3.1), one has shown the highlighted remarkable differences in the obtained predictions, when comparing them with those given by linear models. The results in Section 4.1, relating to the deformation energy, give us important informations about the evolution of the deformative state of the domain $\mathcal{B}$ for each case (either linear and non-linear) showing as the analysis by a non-linear approach implies the possibility to describe relevant and expected phenomena. Also the results show in the Section 4.2 provides an idea of how much more realistic it is to approach the seismic problem with a non-linear modelling. Clearly, the most significative and impactful results for applications are those relating to the accelerations (Section 4.3). These results deserve close attention because high differences are visible and, even more importantly, it clearly shows that the linear approach, almost always, underestimates this quantity. A quantity is the acceleration that represent the most important parameter to consider not only during the study of seismic events but also in anti-seismic structural design. It has to be remarked that a relevant underestimation of experimentally observed accelerations, in the framework of linear theories, seems to have been already underlined in the literature (see EarthQuake Spectra by Luca et al. [33]) Having obtained the prediction for seismic accelerations one can calculate, by means of the fast Fourier transform (using a strong smoothing in order to avoid the peaks generated by numerical errors), the spectrum ratios between the horizontal and vertical accelerations of some specifically chosen points in the considered region (Point 8 and Point 12 in Figure 17) and the horizontal and vertical accelerations spectrum of a reference point (Point 1 in Figure 17); The chosen reference point for spectral ratios is the Point 1 because it stays into the bedrock. These plots are shown at the Figures 30 and 31. Then these ratios have been compared with the Figure 32 that shows the Figure 11 (reproduced here without any change) from Luca et al. [33]. In particular the comparison is carried out with the Figure 11a (for the Point 8 in Figure 30) and the Figure 11b (for the Point 12 in Figure 31). The station named *AQPK*

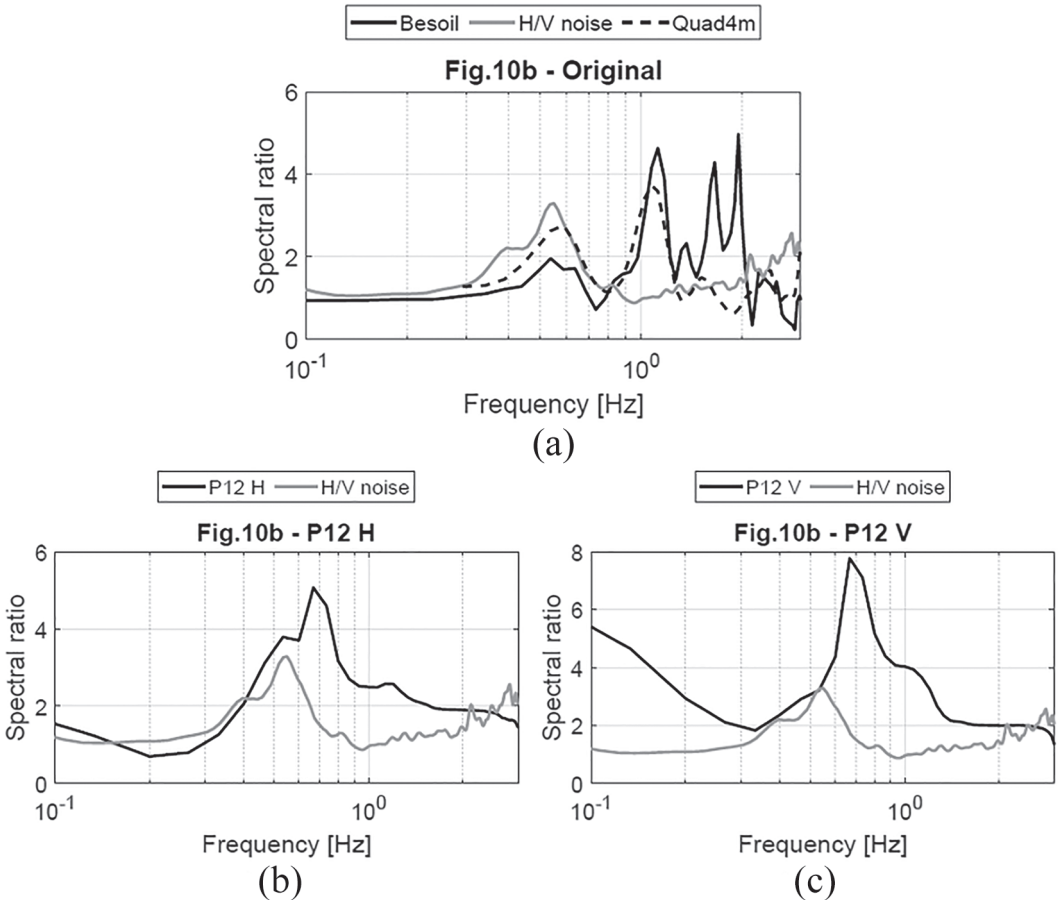

Figure 31. The spectral ratio between the horizontal (b) and vertical (c) non-linear accelerations of the Point 12 and the Point 1 (that is situated into the bedrock, see Figure 17) compared with the Figure 11(b) from Luca et al. [33], shown at the top of the figure (a). The spectral are smoothed with a 50 points moving window.

in Figure 32 is located not far from the Point 8 whereas the station named *GDIF*in Figure 32 is located not far from the Point 12.

Comparing the Figure 30 with the Figure 11(a) by Luca et al. [33], it is clear that the non-linear analysis fits better with the experimental data than the linear analysis. Figure 10(a) and (b) of Luca et al. [33] (both shown in Figure 32) compare QUAD4M and BESOIL results, and confirm that both codes are able to predict the low-frequency amplification peak in the deepest part of the basin. BESOIL solutions are more complex because the code allows higher frequencies. The high-frequency behavior found using BESOIL code cannot be considered physically significant because the model used is not realistic at a small scale. Also the QUAD4M results seem to be less sensitive to frequencies higher than 1.5 Hz because of the grid spacing used. Furthermore, non-linear analysis removes the non-experimentally observed peaks in the frequency range higher than 1Hz that were found by Luca et al. [33], which used the linear codes (*Besoil* and *Quad4m*). The non-linear approach naturally cuts off these peaks. Future analysis will detail the reasons for which this qualitative property of non-linear models holds and will give stronger motivations for the use of spectral ratios to validate continuum models for the "seismic wave propagation" zone studied in the present paper.

A 2D model, while insufficient to fully capture the complex 3D geological structure of the Aterno River Valley, offers a computationally efficient approach to investigate the influence of non-linearity on system behaviour under large excitations. While acknowledging the inherent limitations of such a simplification, we argue that this 2D model effectively demonstrates the significant role of non-linearity. Future investigations will need to refine the just mentioned analysis, by introducing a careful and more realistic

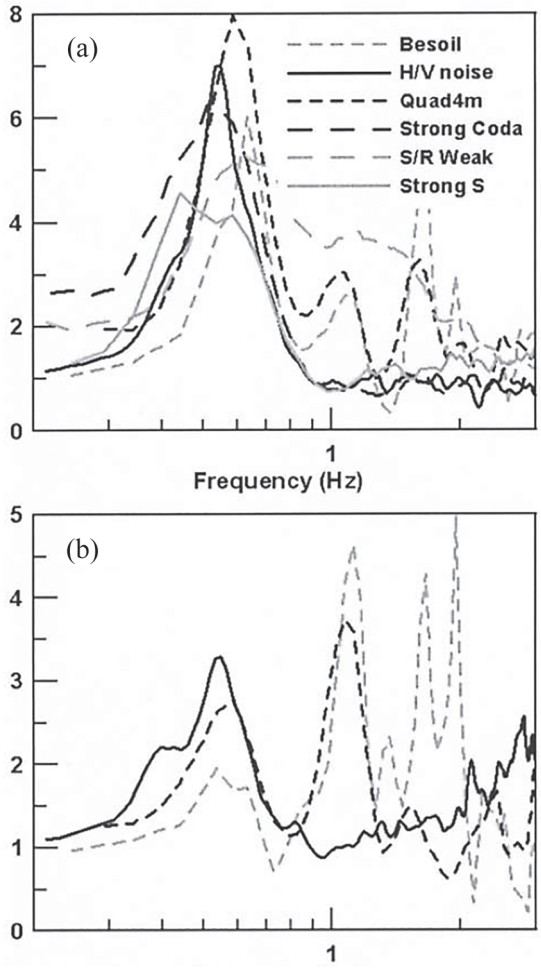

Figure 32. Figure 11 from Luca et al. [33] (figure and caption are not modified): *"(a) QUAD4M and BESOIL solutions compared with H/V applied to strong-motion and microtremor data and S/R applied to weak-motion data at the AQPK site. (b) QUAD4M and BESOIL solutions compared with H/V applied to microtremor data at the GDIF site. The line symbol are the same in both (a) and (b)"*

3D modelling, developing appropriate numerical method for non-linear system [120,121], enlarging the region where wave propagation is studied, in order to include the sites where other accelerometer stations of National Survey Network of Civil Protection were localised. These stations have been active since the middle of 1990s and have recorded a large number of earthquakes having different magnitude and hypocenters. Moreover in order to get a careful prediction of origins and onset of the seismic actions, from a geological and mechanical point of view, models of tectonic dynamic crack propagation must be considered, generalising and adapting the methods presented by Barchiesi et al. [122], Fabbrocino et al. [123], Placidi and Barchiesi [124], Placidi et al. [125], Turco et al. [126]. In this way, it will be possible to extend the regions where wave propagation is predicted, to include also hypocenters. We also expect that the presented results will allow for a more effective design for the new structures (and for the restoration of the damaged one) by exploiting the also knowledge and the conceptual tools which are already available and were used, e.g., by Masi et al. [127], Saitta et al. [128], Salvatori [129]. In conclusion, it is clearly well-established that the computational cost associated with non-linear analysis is significantly higher than that of linear one. Consequently, it is reasonable to question the extent to which such computational demands are justified in the study of seismic phenomena. However, the results obtained from our non-linear analysis provide compelling evidence to support this approach. These findings cannot be disregarded and warrant careful consideration, as they offer a more accurate means of predicting the effects of high-energy seismic events given the current state of technology. As long as our non-linear

models continue to yield results that deviate significantly from those obtained through linear analysis, while simultaneously demonstrating a high degree of agreement with experimental data, we believe that further refinement of these models is warranted. Such refinements are essential for enhancing the safety of human life and improving the design of structures.

Funding

The author(s) received no financial support for the research, authorship, and/or publication of this article.

ORCID iDs

Ivan Giorgio https://orcid.org/0000-0002-0044-9188
Luca Placidi https://orcid.org/0000-0002-1461-3997

References

[1] Eremeyev, VA, Alzahrani, FS, Cazzani, A, et al. On existence and uniqueness of weak solutions for linear pantographic beam lattices models. *Continuum Mech Therm* 2019; 31(6): 1843–1861.
[2] Ciallella, A, Pasquali, D, D'Annibale, F, et al. Shear rupture mechanism and dissipation phenomena in bias-extension test of pantographic sheets: numerical modeling and experiments. *Math Mech Solids* 2022; 27(10): 2170–2188.
[3] Laudato, M, and Barchiesi, E. Non-linear dynamics of pantographic fabrics: modelling and numerical study. In: Sumbatyan, MA (ed.) *Wave dynamics, mechanics and physics of microstructured metamaterials: Theoretical and experimental methods*. Cham: Springer, 2019, pp. 241–254.
[4] dell'isola, F, Corte, AD, Battista, A, et al. Extensible beam models in large deformation under distributed loading: a numerical study on multiplicity of solutions. In: Altenbach, H, Müller, WH, and Abali, BE (eds) *Higher gradient materials and related generalized continua*. Cham: Springer, 2019, pp. 19–41.
[5] Eremeyev, V, and Zubov, L. On constitutive inequalities in nonlinear theory of elastic shells. *J Appl Math Mech* 2007; 87(2): 94–101.
[6] Abali, BE, Müller, WH, and Eremeyev, VA. Strain gradient elasticity with geometric nonlinearities and its computational evaluation. *Mech Adv Mater Modern Process* 2015; 1(1): 1–11.
[7] Eremeyev, VA, Cazzani, A, and Dell'isola, F. On nonlinear dilatational strain gradient elasticity. *Continuum Mech Therm* 2021; 33(4): 1429–1463.
[8] Eremeyev, VA, and Pietraszkiewicz, W. The nonlinear theory of elastic shells with phase transitions. *J Elasticity* 2004; 74(1): 67–86.
[9] Eugster, SR. Numerical analysis of nonlinear wave propagation in a pantographic sheet. *Math Mech Complex Syst* 2022; 9(3): 293–310.
[10] Turco, E, Barchiesi, E, Ciallella, A, et al. Nonlinear waves in pantographic beams induced by transverse impulses. *Wave Motion* 2022; 115: 103064.
[11] Eremeyev, VA, Lebedev, LP, and Cloud, MJ. Acceleration waves in the nonlinear micromorphic continuum. *Mech Res Commun* 2018; 93: 70–74.
[12] Abd-alla, A, Alshaikh, F, Giorgio, I, et al. A mathematical model for longitudinal wave propagation in a magnetoelastic hollow circular cylinder of anisotropic material under the influence of initial hydrostatic stress. *Math Mech Solids* 2016; 21(1): 104–118.
[13] Abali, BE, and Barchiesi, E. Additive manufacturing introduced substructure and computational determination of metamaterials parameters by means of the asymptotic homogenization. *Continuum Mech Therm* 2021; 33(4): 993–1009.
[14] Cefis, N, Fedele, R, and Beghi, MG. An integrated methodology to estimate the effective elastic parameters of amorphous tio2 nanostructured films, combining sem images, finite element simulations and homogenization techniques. *Mech Res Commun* 2023; 131: 104153.
[15] Fedele, R, and Maier, G. Flat-jack tests and inverse analysis for the identification of stress states and elastic properties in concrete dams. *Meccanica* 2007; 42(4): 387–402.
[16] Fedele, R, Sessa, S, and Valoroso, N. Image correlation-based identification of fracture parameters for structural adhesives. *Tech Mech-Eur J Eng Mech* 2019; 32(2–5): 195–204.
[17] Darban, H, Luciano, R, Caporale, A, et al. Higher modes of buckling in shear deformable nanobeams. *Int J Eng Sci* 2020; 154: 103338.
[18] Bormann, P, Baumbach, M, Bock, G, et al. Seismic sources and source parameters. In: Bormann P (ed.) *New manual of seismological observatory practice (NMSOP-1)*. Potsdam: Deutsches GeoForschungsZentrum GFZ, 2009, pp. 1–94.
[19] Turco, E, and Barchiesi, E. Kinematically-triggered nonlinear vibrations of Hencky-type pantographic sheets. *Math Mech Complex Syst* 2021; 9: 311–335.

[20] Luciano, R, Darban, H, Bartolomeo, C, et al. Free flexural vibrations of nanobeams with non-classical boundary conditions using stress-driven nonlocal model. *Mech Res Commun* 2020; 107: 103536.
[21] Mancusi, G, Fabbrocino, F, Feo, L, et al. Size effect and dynamic properties of 2D lattice materials. *Compos B Eng* 2017; 112: 235–242.
[22] Funari, MF, Spadea, S, Fabbrocino, F, et al. A moving interface finite element formulation to predict dynamic edge debonding in FRP-strengthened concrete beams in service conditions. *Fibers* 2020; 8(6): 42.
[23] Turco, E, and Barchiesi, E. Kinematically triggered nonlinear vibrations of Hencky-type pantographic sheets. *Math Mech Complex Syst* 2022; 9(3): 311–335.
[24] Javili, A, Dell'isola, F, and Steinmann, P. Geometrically nonlinear higher-gradient elasticity with energetic boundaries. *J Mech Phys Solids* 2013; 61(12): 2381–2401.
[25] Placidi, L, Barchiesi, E, Dell'isola, F, et al. On a hemi-variational formulation for a 2D elasto-plastic-damage strain gradient solid with granular microstructure. *Math Eng* 2022; 5: 1–24.
[26] Scrofani, A, Barchiesi, E, Chiaia, B, et al. Fluid diffusion related aging effect in a concrete dam modeled as a Timoshenko beam. *Math Mech Complex Syst* 2023; 11(2): 313–334.
[27] Chiaia, B, Biagi, VD, and Placidi, L. A damaged non-homogeneous Timoshenko beam model for a dam subjected to aging effects. *Math Mech Solids* 2021; 26(5): 694–707.
[28] Luca, GD, Scarpa, R, Filippi, L, et al. A detailed analysis of two seismic sequences in Abruzzo, Central Apennines, Italy. *J Seismol* 2000; 4(1): 1–21.
[29] Scognamiglio, L, Tinti, E, and Quintiliani, M. Time Domain Moment Tensor (TDMT) [Data set]. Istituto Nazionale di Geofisica e Vulcanologia (INGV), 2006. DOI: 10.13127/TDMT.
[30] Chiarabba, C, Amato, A, Anselmi, M, et al. The 2009 L'Aquila (Central Italy) mw6.3 earthquake: main shock and aftershocks. *Geophys Res Lett* 2009; 36(18): 1–6.
[31] Rovida, A, Locati, M, Camassi, R, et al. Catalogo Parametrico dei Terremoti Italiani (CPTI15), versione 4.0 [Data set]. Istituto Nazionale di Geofisica e Vulcanologia (INGV), 2022. DOI: 10.13127/cpti/cpti15.4.
[32] Rovida, A, Locati, M, Camassi, R, et al. The Italian earthquake catalogue CPTI15. *B Earthq Eng* 2020; 18(7): 2953–2984.
[33] Luca, GD, Marcucci, S, Milana, G, et al. Evidence of low-frequency amplification in the city of L'Aquila, Central Italy, through a multidisciplinary approach including strong- and weak-motion data, ambient noise, and numerical modelling. *Bull Seismol Soc Am* 2005; 95(4): 1469–1481.
[34] Milana, G, Azzara, RM, Bertrand, E, et al. The contribution of seismic data in microzonation studies for downtown L'Aquila. *B Earthq Eng* 2011; 9(3): 741–759.
[35] Puglia, R, Ditommaso, R, Pacor, F, et al. Frequency variation in site response as observed from strong motion data of the L'Aquila (2009) seismic sequence. *B Earthq Eng* 2011; 9(3): 869–892.
[36] Ragozzino, E. Nonlinear seismic response in the western L'Aquila basin (Italy): numerical FEM simulations vs. ground motion records. *Eng Geol* 2014; 174: 46–60.
[37] Ferraro, A, Grasso, S, Maugeri, M, et al. Seismic response analysis in the southern part of the historic centre of the city of L'Aquila (Italy). *Soil Dyn Earthq Eng* 2016; 88: 256–264.
[38] Giulio, GD, Gaudiosi, I, Cara, F, et al. Shear-wave velocity profile and seismic input derived from ambient vibration array measurements: the case study of downtown L'Aquila. *Geophys J Int* 2014; 198: 848–866.
[39] Tallini, M, Sardo, LL, and Spadi, M. Seismic site characterisation of red soil and soil-building resonance effects in L'Aquila downtown (Central Italy). *Bull Eng Geol Environ* 2020; 79(8): 4021–4034.
[40] Bergamaschi, F, Cultrera, G, Azzara, R, et al. Evaluation of site effects in the Aterno river valley (Central Italy) from aftershocks of the 2009 L'Aquila earthquake. *B Earthq Eng* 2011; 9: 697–715.
[41] Calderoni, G, Rovelli, A, and Giovambattista, RD. Large amplitude variations recorded by an on-fault seismological station during the L'Aquila earthquakes: evidence for a complex fault-induced site effect. *Geophys Res Lett* 2010; 37: L24305.
[42] Akinci, A, Malagnini, L, and Sabetta, F. Characteristics of the strong ground motions from the 6 April 2009 L'Aquila earthquake, Italy. *Soil Dyn Earthq Eng* 2010; 30(5): 320–335.
[43] Lanzo, G, and Pagliaroli, A. Seismic site effects at near-fault strong-motion stations along the Aterno River Valley during the Mw=6.3 2009 L'Aquila earthquake. *Soil Dyn Earthq Eng* 2012; 40: 1–14.
[44] Bindi, D, Pacor, F, Luzi, L, et al. The Mw 6.3, 2009 L'Aquila earthquake: source, path and site effects from spectral analysis of strong motion data. *Geophys J Int* 2009; 179(3): 1573–1579.
[45] Ameri, G, Bindi, D, Pacor, F, et al. The 2009 April 6, Mw 6.3, L'Aquila (Central Italy) earthquake: finite-fault effects on intensity data. *Geophys J Int* 2011; 186(2): 837–851.
[46] Ugurhan, B, Askan, A, Akinci, A, et al. Strong-ground-motion simulation of the 6 April 2009 L'Aquila, Italy, earthquake. *Bull Seismol Soc Am* 2012; 102(4): 1429–1445.
[47] Felicetta, C, Russo, E, D'Amico, M, et al. Italian Accelerometric Archive v4.0. Istituto Nazionale di Geofisica e Vulcanologia, Dipartimento della Protezione Civile Nazionale, 2023. DOI: 10.13127/itaca.4.0.
[48] Celebi, M, Bazzurro, P, Chiaraluce, L, et al. Recorded motions of the 6 April 2009 Mw 6.3 L'Aquila, Italy, earthquake and implications for building structural damage: overview. *Earthq Spectra* 2010; 26(3): 651–684.

[49] Stewart, JP, Lanzo, G, Pagliaroli, A, et al. Ground motion recordings from the Mw 6.3 2009 L'Aquila earthquake in Italy and their engineering implications. *Earthq Spectra* 2012; 28(1): 317–345.
[50] Rupakhety, R, and Sigbjörnsson, R. A note on the L'Aquila earthquake of 6 April 2009: permanent ground displacements obtained from strong-motion accelerograms. *Soil Dyn Earthq Eng* 2010; 30(4): 215–220.
[51] Augenti, N, and Parisi, F. Learning from construction failures due to the 2009 L'Aquila, Italy, earthquake. *J Perform Constr Fac* 2010; 24: 536–555.
[52] Cucci, L, and Tertulliani, A. Clues for a relation between rotational effects induced by the 2009 Mw 6.3 L'Aquila (Central Italy) earthquake and site and source effects. *B Seismol Soc Am* 2011; 101: 1109–1120.
[53] Tertulliani, A, Leschiutta, I, Bordoni, P, et al. Damage distribution in L'Aquila city (Central Italy) during the 6 April 2009 earthquake. *Bull Seismol Soc Am* 2012; 102(4): 1543–1553.
[54] Mannella, A, Macerola, L, Martinelli, A, et al. The local seismic response and the effects of the 2016 Central Italy earthquake on the buildings of L'Aquila downtown. *Boll Geofis Teor Appl* 2019; 60(2): 263–276.
[55] Douglas, J, Monfort, D, Negulescu, C, et al. Limits on the potential accuracy of earthquake risk evaluations using the L'Aquila (Italy) earthquake as an example. *Ann Geophys* 2015; 58: S0214.
[56] Vannoli, P, Burrato, P, and Valensise, G. The seismotectonics of the Po Plain (Northern Italy): tectonic diversity in a blind faulting domain. *Pure Appl Geophys* 2015; 172: 1105–1142.
[57] Tertulliani, A, Arcoraci, L, Berardi, M, et al. An application of EMS98 in a medium-sized city: the case of L'Aquila (Central Italy) after the April 6, 2009 Mw 6.3 earthquake. *B Earthq Eng* 2011; 9: 67–80.
[58] Blumetti, AM, Manna, PD, Comerci, V, et al. Paleoseismicity of the San Demetrio ne' Vestini fault (L'Aquila Basin, Central Italy): implications for seismic hazard. *Quatern Int* 2017; 451: 129–142.
[59] Bruno, PPG, Villani, F, and Improta, L. High-resolution seismic imaging of fault-controlled basins: a case study from the 2009 Mw 6.1 Central Italy earthquake. *Tectonics* 2022; 41(4): e2022TC007207.
[60] Civico, R, Sapia, V, Giulio, GD, et al. Geometry and evolution of a fault-controlled quaternary basin by means of TDEM and single-station ambient vibration surveys: the example of the 2009 L'Aquila earthquake area, Central Italy. *J Geophys Res Solid Earth* 2017; 122(3): 2236–2259.
[61] Nocentini, M, Cosentino, D, Spadi, M, et al. Plio-Quaternary geology of the Paganica-San Demetrio-Castelnuovo Basin (Central Italy). *J Maps* 2018; 14: 411–420.
[62] Spadi, M, Tallini, M, Albano, M, et al. New insights on bedrock morphology and local seismic amplification of the castelnuovo village (L'Aquila Basin, Central Italy). *Eng Geol* 2022; 297: 106506.
[63] Tallini, M, Spadi, M, Cosentino, D, et al. High-resolution seismic reflection exploration for evaluating the seismic hazard in a Plio-Quaternary intermontane basin (L'Aquila downtown, Central Italy). *Quatern Int* 2019; 532: 34–47.
[64] Cultrera, G, Mucciarelli, M, and Parolai, S. The L'Aquila earthquake—a view of site effects and building behavior from temporary networks. *B Earthq Eng* 2011; 9(3): 691–695.
[65] Monaco, P, and Amoroso, S. Site effects from the building scale to the seismic microzonation scale: examples from the experience of L'Aquila. *Procedia Engineer* 2016; 158: 517–522.
[66] Nunziata, C, and Costanzo, M. Ground motion modeling for site effects at L'Aquila and middle Aterno river valley (Central Italy) for the Mw 6.3, 2009 earthquake. *Soil Dyn Earthq Eng* 2014; 61–62: 107–123.
[67] Nunziata, C, Vaccari, F, and Panza, GF. The Mw 6.3, 2009 LAquila earthquake: Linear and nonlinear site effects. In: Mazzolani FM (ed.) *Urban Habitat Constructions Under Catastrophic Events: Proceedings of the Cost C26 Action Final Conference*. London: Taylor & Francis Group, 2010.
[68] Nunziata, C, Costanzo, M, Vaccari, F, et al. Evaluation of linear and nonlinear site effects for the MW 6.3, 2009 L'Aquila earthquake. *Earthquake Research and AnalysiseNew Frontiers in Seismology* 2012; 5: 155e176.
[69] Magnoni, F, Casarotti, E, Michelini, A, et al. Spectral-element simulations of seismic waves generated by the 2009 L'Aquila earthquake. *Bull Seismol Soc Am* 2014; 104(1): 73–94.
[70] Smerzini, C, and Villani, M. Broadband numerical simulations in complex near-field geological configurations: the case of the 2009 Mw 6.3 L'Aquila earthquake. *Bull Seismol Soc Am* 2012; 102(6): 2436–2451.
[71] Michele, FD, May, J, Pera, D, et al. Spectral element numerical simulation of the 2009 L'Aquila earthquake on a detailed reconstructed domain. *Geophys J Int* 2022; 230(1): 29–49.
[72] Gaudiosi, I, Monaco, FD, Milana, G, et al. Site effects in the Aterno river valley (L'Aquila, Italy): comparison between empirical and 2D numerical modelling starting from April 6th 2009 Mw 6.3 earthquake. *B Earthq Eng* 2014; 12(2): 697–716.
[73] Margheriti, L, Chiaraluce, L, Voisin, C, et al. Rapid response seismic networks in Europe: lessons learnt from the L'Aquila earthquake emergency. *Ann Geophys* 2011; 54: 392–399.
[74] Barchi, M, Lavecchia, G, Galadini, F, et al. Sintesi delle conoscenze sulle faglie attive in italia centrale: Parametrizzazione ai fini della caratterizzazione della pericolosità sismica, 2000.
[75] Carminati, E, Lustrino, M, Cuffaro, M, et al. Tectonics, magmatism and geodynamics of Italy: what we know and what we imagine, in: Beltrando, M., Peccerillo, A., Mattei, M., Conticelli, S., Doglioni, C. (Eds.), The Geology of Italy: tectonics and life along plate margins. *J Virtual Expl, Electronic Edition* 2010; 36: 1441–8142.

[76] Cavinato, GP, P, G, and Celles, PGD. Extensional basins in the tectonically bimodal central apennines fold-thrust belt, Italy: response to corner flow above a subducting slab in retrograde motion. *Geology* 1999; 27(10): 955–958.
[77] Cosentino, D, Asti, R, Nocentini, M, et al. New insights into the onset and evolution of the central apennine extensional intermontane basins based on the tectonically active L'Aquila basin (Central Italy). *Bull Cl Sci Math Nat Sci Math* 2017; 129(9–10): 1314–1336.
[78] Boncio, P, Lavecchia, G, and Pace, B. Defining a model of 3D seismogenic sources for seismic hazard assessment applications: the case of central apennines (Italy). *J Seismol* 2004; 8(9–10): 407–425.
[79] Devoti, R, Pietrantonio, G, Pisani, AR, et al. Present day kinematics of Italy. *J Virtual Expl* 2010; 36(2): 1–14.
[80] Pondrelli, S, Salimbeni, S, Ekström, G, et al. The Italian CMT dataset from 1977 to the present. *Phys Earth Planet Inter* 2006; 159(3): 286–303.
[81] Galadini, F, and Galli, P. Active tectonics in the central Apennines (Italy) – input data for seismic hazard assessment. *Nat Hazards* 2000; 22(3): 225–268.
[82] Malikan, M, and Eremeyev, VA. On time-dependent nonlinear dynamic response of micro-elastic solids. *Int J Eng Sci* 2023; 182: 103793.
[83] Apuzzo, A, Barretta, R, Fabbrocino, F, et al. Axial and torsional free vibrations of elastic nano-beams by stress-driven two-phase elasticity. *J Appl Comput Mech* 2019; 5(2): 402–413.
[84] Barretta, R, Faghidian, SA, and Luciano, R. Longitudinal vibrations of nano-rods by stress-driven integral elasticity. *Mech Adv Mater Struc* 2019; 26(15): 1307–1315.
[85] Heiduschke, K. On tensor projections, stress or stretch vectors and their relations to Mohr's three circles. *Math Mech Complex Syst* 2024; 12(2): 173–216.
[86] Sharma, BL, and Eremeyev, VA. Wave transmission across surface interfaces in lattice structures. *Int J Eng Sci* 2019; 145: 103173.
[87] Placidi, L, Girolamo, FD, and Fedele, R. Variational study of a Maxwell–Rayleigh-type finite length model for the preliminary design of a tensegrity chain with a tunable band gap. *Mech Res Commun* 2024; 136: 104255.
[88] Placidi, L, Sherbiny, MGE, and Baragatti, P. Experimental investigation for the existence of frequency band gap in a microstructure model. *Math Mech Complex Syst* 2022; 9(4): 413–421.
[89] Mikhasev, G, Erbaş, B, and Eremeyev, VA. Anti-plane shear waves in an elastic strip rigidly attached to an elastic half-space. *Int J Eng Sci* 2023; 184: 103809.
[90] Askes, H, and Wallace, AR. Dynamic Bergan–Wang theory for thick plates. *Math Mech Complex Syst* 2022; 10(2): 191–204.
[91] Ko, KY, and Solyaev, Y. Explicit benchmark solution for topology optimization of variable-thickness plates. *Math Mech Complex Syst* 2023; 11(3): 381–392.
[92] Andreaus, U, dell'isola, F, Giorgio, I, et al. Numerical simulations of classical problems in two-dimensional (non) linear second gradient elasticity. *Int J Eng Sci* 2016; 108: 34–50.
[93] dell'isola, F, Eugster, SR, Fedele, R, et al. Second-gradient continua: from Lagrangian to Eulerian and back. *Math Mech Solids* 2022; 27(12): 2715–2750.
[94] Solyaev, Y, Lurie, S, Barchiesi, E, et al. On the dependence of standard and gradient elastic material constants on a field of defects. *Math Mech Solids* 2020; 25(1): 35–45.
[95] Placidi, L, Rosi, G, Giorgio, I, et al. Reflection and transmission of plane waves at surfaces carrying material properties and embedded in second-gradient materials. *Math Mech Solids* 2014; 19(5): 555–578.
[96] Rosi, G, Giorgio, I, and Eremeyev, VA. Propagation of linear compression waves through plane interfacial layers and mass adsorption in second gradient fluids. *J Appl Math Mech* 2013; 93(12): 914–927.
[97] Yang, B, Bacciocchi, M, Fantuzzi, N, et al. Wave propagation in periodic nano structures through second strain gradient elasticity. *Int J Mech Sci* 2023; 260: 108639.
[98] Cornacchia, F, Fabbrocino, F, Fantuzzi, N, et al. Analytical solution of cross- and angle-ply nano plates with strain gradient theory for linear vibrations and buckling. *Mech Adv Mater Struc* 2021; 28(12): 1201–1215.
[99] Cuomo, M, Contrafatto, L, and Greco, L. A cohesive interface model with degrading friction coefficient. *Math Mech Complex Syst* 2024; 12(2): 113–133.
[100] Ponomarev, D. A generalised time-evolution model for contact problems with wear and its analysis. *Math Mech Complex Syst* 2022; 10(3): 279–319.
[101] Grillo, A, and Stefano, SD. An a posteriori approach to the mechanics of volumetric growth. *Math Mech Complex Syst* 2023; 11(1): 57–86.
[102] Grillo, A, and Stefano, SD. Comparison between different viewpoints on bulk growth mechanics. *Math Mech Complex Syst* 2023; 11(2): 287–311.
[103] Tepedino, M. The mechanical role of the periodontal ligament for developing mathematical models in orthodontics. *Math Mech Complex Syst* 2023; 11(4): 525–539.
[104] Olive, M, and Auffray, N. Symmetry classes in piezoelectricity from second-order symmetries. *Math Mech Complex Syst* 2021; 9: 77–105.
[105] Misra, A, Placidi, L, Dell'isola, F, et al. Identification of a geometrically nonlinear micromorphic continuum via granular micromechanics. *Z fur Angew Math Physik* 2021; 72(4): 157.

[106] Sciarra, G, dell'Isola, F, and Coussy, O. Second gradient poromechanics. *Int J Solids Struct* 2007; 44(20): 6607–6629.
[107] Timofeev, D, Barchiesi, E, Misra, A, et al. Hemivariational continuum approach for granular solids with damage-induced anisotropy evolution. *Math Mech Solids* 2021; 26(5): 738–770.
[108] Turco, E, dell'Isola, F, and Misra, A. A nonlinear Lagrangian particle model for grains assemblies including grain relative rotations. *Int J Numer Anal Met* 2019; 43(5): 1051–1079.
[109] Placidi, L, Barchiesi, E, Dell'isola, F, et al. A granular-based elasto-plastic–damage energy formulation for strain gradient solids. In: *Book of Abstracts*, 2021.
[110] Barchiesi, E, Misra, A, Placidi, L, et al. Identification, based on granular micromechanics, of elastic isotropic strain gradient stiffness matrices for geometrically nonlinear deformations, 2021. Available at: https://iris.uninettunouniversity.net/handle/20.500.14086/2320
[111] Nocentini, M, Asti, R, Cosentino, D, et al. Plio-quaternary geology of L'Aquila–Scoppito Basin (Central Italy). *J Maps* 2017; 13.2: 563–574.
[112] Antonielli, B, Seta, MD, Esposito, C, et al. Quaternary rock avalanches in the Apennines: new data and interpretation of the huge clastic deposit of the L'Aquila basin (Central Italy). *Geomorphology* 2020; 361: 107194.
[113] Blumetti, AM. Neotectonic investigations and evidence of paleoseismicity in the epicentral area of the January–February 1703, Central Italy, earthquakes. *Perspect Paleoseismol* 1995; 6: 83–100.
[114] Bruyelle, P. Jean Demangeot—Géomorphologie des Abruzzes adriatiques. Thèse pour le doctorat ès-lettres. Centre de Recherches et documentation cartographique et géographiques, n° hors-série-1965. *Hommes terres nord* 1966; 1(1): 120–121.
[115] Giorgio, I. A variational formulation for one-dimensional linear thermoviscoelasticity. *Math Mech Complex Syst* 2022; 4(9): 397–412.
[116] Bersani, AM, Caressa, P, and Ciallella, A. Numerical evidence for the approximation of dissipative systems by gyroscopically coupled oscillator chains. *Math Mech Complex Syst* 2022; 10(3): 265–278.
[117] Eremeyev, VA. Surface finite viscoelasticity and surface anti-plane waves. *Int J Eng Sci* 2024; 196: 104029.
[118] Barchiesi, E, Misra, A, Placidi, L, et al. Granular micromechanics-based identification of isotropic strain gradient parameters for elastic geometrically nonlinear deformations. *Z Angew Math Mech* 2021; 101(11): 1–21.
[119] Soize, C. An overview on uncertainty quantification and probabilistic learning on manifolds in multiscale mechanics of materials. *Math Mech Complex Syst* 2023; 11(1): 87–174.
[120] Salnikov, V. On numerical approaches to the analysis of topology of the phase space for dynamical integrability. *Chaos Solitons Fractals* 2013; 57: 155–161.
[121] Salnikov, V, and Hamdouni, A. From modelling of systems with constraints to generalized geometry and back to numerics. *J Appl Math Mech* 2019; 99(6): e201800218.
[122] Barchiesi, E, Yang, H, Tran, C, et al. Computation of brittle fracture propagation in strain gradient materials by the fenics library. *Math Mech Solids* 2021; : 325–340.
[123] Fabbrocino, F, Funari, MF, Greco, F, et al. Dynamic crack growth based on moving mesh method. *Compos B Eng* 2019; 174: 107053.
[124] Placidi, L, and Barchiesi, E. Energy approach to brittle fracture in strain-gradient modelling. *Proc R Soc A Math Phys Eng Sci* 2018; 474: 20170878.
[125] Placidi, L, Misra, A, and Barchiesi, E. Simulation results for damage with evolving microstructure and growing strain gradient moduli. *Continuum Mech Therm* 2019; 31(4): 1143–1163.
[126] Turco, E, Barchiesi, E, Ciallella, A, et al. A new block-based approach for the analysis of damage in masonries undergoing large deformations. *Continuum Mech Therm* 2023; 35: 1625–1654.
[127] Masi, A, Manfredi, V, Vona, M, et al. Prestazioni delle tamponature e tramezzature negli edifici in c.a.: implicazioni progettuali e costruttive alla luce dell'esperienza del terremoto dell'abruzzo 2009. *Progettazione Sismica* 2009; 3: 51–66.
[128] Saitta, F, Clemente, P, Buffarini, G, et al. Base isolation of buildings with curved surface sliders: basic design criteria and critical issues. *Adv Civil Eng* 2018; 2018: 1569683.
[129] Salvatori, A. Seismic base isolation: retrofitting application in structures damaged by earthquake. In: *Proceedings of 16th European conference on earthquake engineering ECEE*, Thessaloniki, Greece, 18-21 June, 2018.